Spectral Energy Dissipation due to Surface Wave Breaking

LEONEL ROMERO AND W. KENDALL MELVILLE
Scripps Institution of Oceanography, La Jolla, California

JESSICA M. KLEISS
Joint Institute for the Study of the Atmosphere and Ocean, University of Washington, Seattle, Washington

(Manuscript received 7 April 2011, in final form 13 December 2011)

ABSTRACT

A semiempirical determination of the spectral dependence of the energy dissipation due to surface wave breaking is presented and then used to propose a model for the spectral dependence of the breaking strength parameter b, defined in the O. M. Phillips's statistical formulation of wave breaking dynamics. The determination of the spectral dissipation is based on closing the radiative transport equation for fetch-limited waves, measured in the Gulf of Tehuantepec Experiment, by using the measured evolution of the directional spectra with fetch, computations of the four-wave resonant interactions, and three models of the wind input source function. The spectral dependence of the breaking strength is determined from the Kleiss and Melville measurements of the breaking statistics and the semiempirical spectral energy dissipation, resulting in $b = b(k, c_p/u_*)$, where k is the wavenumber and the parametric dependence is on the wave age, c_p/u_*. Guided by these semiempirical results, a model for $b(k, c_p/u_*)$ is proposed that uses laboratory data from a variety of sources, which can be represented by $b = a(S - S_0)^n$, where S is a measure of the wave slope at breaking, a is a constant, S_0 is a threshold slope for breaking, and $2.5 < n < 3$ is a power law consistent with inertial wave dissipation scaling and laboratory measurements. The relationship between $b(S)$ in the laboratory and $b(k)$ in the field is based on the relationship between the saturation and mean square slope of the wave field. The results are discussed in the context of wind wave modeling and improved measurements of breaking in the field.

1. Introduction

Breaking wind waves play an important role in air–sea interaction processes including the exchange of energy, momentum, heat, and gases between the ocean and the atmosphere; mixing of the upper ocean and aerosol production (Melville 1996). Many of the present parameterizations of air–sea fluxes rely on empirical relationships of the fractional whitecap coverage versus the wind speed, typically referenced to 10 m above mean sea level (U_{10}), without information about the wind wave spectrum or the spectral energy dissipation.

Recent advances in image-processing techniques, using digitally acquired images of breaking waves, have allowed the visual detection and quantification of the length and velocity of breaking fronts, providing estimates of Phillips' (1985) $\Lambda(\mathbf{c})$, the length of breaking fronts with velocities in the range ($\mathbf{c}$, $\mathbf{c} + d\mathbf{c}$) per unit surface area. See, for example, Melville and Matusov (2002, hereafter MM); Gemmrich et al. (2008); Thomson et al. (2009); and more recently, for the Gulf of Tehuantepec Experiment (GOTEX), Kleiss and Melville (2010, 2011). Following Phillips, the first, fourth, and fifth moments of $\Lambda(\mathbf{c})$ are proportional to the breaking rate, wave momentum flux lost to the upper-ocean surface currents, and energy lost from the wave field due to wave breaking. As shown by Kleiss and Melville (2010), the second moment can be related to the active whitecap coverage, which is the fractional area covered by actively breaking waves. Thus, $\Lambda(\mathbf{c})$ and its moments provide a framework to relate the energy and momentum balances to the breaking rate and active whitecap coverage, which would allow present numerical wind wave models to predict the wave breaking statistics more accurately than the traditional parameterizations that depend on U_{10} and, in some cases, air–sea temperature differences.

Corresponding author address: Leonel Romero, Earth Research Institute, University of California, Santa Barbara, Santa Barbara, CA 93106-3060.
E-mail: leromero@eri.ucsb.edu

DOI: 10.1175/JPO-D-11-072.1

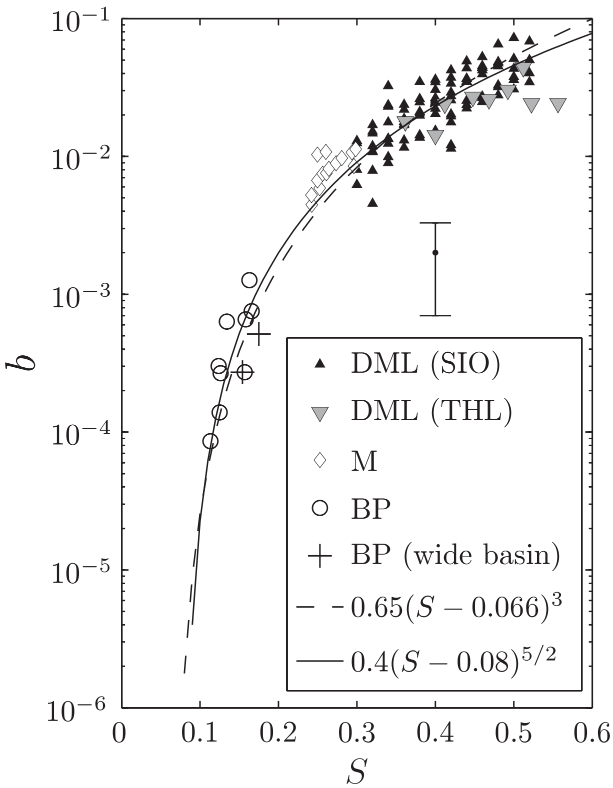

FIG. 1. Laboratory observations of the breaking parameter b as a function of the predicted linear maximum slope S of the focusing wave packet. The data by Banner and Peirson (2007) are shown with circles and pluses. The open diamonds show the data from Melville (1994) using results from earlier experiments at the Massachusetts Institute of Technology. The black and gray triangles (DML) are the data in Drazen et al. (2008) from experiments conducted at Scripps Institution of Oceanography (SIO) and Tainan Hydraulics Laboratory (THL), Taiwan, respectively. The bar shows the average error of the field data for $b(k)$ shown in Fig. 14. The dashed and solid lines are given by Eqs. (23) and (24).

Specifically, the spectral energy dissipation is related to the fifth moment of $\Lambda(\mathbf{c})$ by

$$\rho_w g S_{\rm ds}(\mathbf{c})\, d\mathbf{c} = \rho_w \frac{b}{g}\Lambda(\mathbf{c})c^5\, d\mathbf{c}, \qquad (1)$$

where ρ_w is the density of water; g is gravity; $S_{\rm ds}(\mathbf{c})$ is the wave energy dissipation; $\mathbf{c}$ and c are the wave phase velocity and speed, respectively; and b is the dimensionless breaking parameter, which is a measure of the strength of breaking and was initially measured in laboratory experiments (Melville 1994). Figure 1 shows the data from several laboratory measurements (Melville 1994; Banner and Peirson 2007; Drazen et al. 2008) showing b as a function of S, where S is the predicted maximum linear slope of focusing wave packets (Drazen et al. 2008). The data show that b is not constant, varying by more than three orders of magnitude, ranging between 8×10^{-5} and 9×10^{-2} for gently spilling to plunging waves.

In this study a semiempirical model of the spectral energy dissipation is presented. The model follows Phillips (1985), by solving for the spectral dissipation from the energy balance—in this case using novel airborne observations of winds and waves in fetch-limited conditions, collected during GOTEX (Melville et al. 2005; Romero and Melville 2010a), three parameterizations of the wind input, and ''exact'' computations of the nonlinear energy transfer due to four-wave resonant interactions. The model dissipation and the measurements of $\Lambda(c)$ (Kleiss and Melville 2010) are used to calculate and model a spectral function $b(k)$ that characterizes the strength of wave breaking across the spectrum. Section 2 provides background information. Section 3 describes the semiempirical model and presents the spectral breaking parameter $b(k)$. In section 4 two models of $b(k)$ are proposed and fitted to the data. In section 5 the results are discussed, and the conclusions are given in section 6.

2. Background

This study is concerned with the spectral energy dissipation of fetch-limited deep-water waves due to breaking. Neglecting any gradients of the surface currents, the evolution of the directional spectrum $F(k, \theta)$ is described through the radiative transport equation:

$$\frac{\partial F(k,\theta)}{\partial t} + (\mathbf{c}_g + \mathbf{u}_c)\cdot\nabla F(k,\theta) = S_{\rm in} + S_{\rm nl} + S_{\rm ds}, \quad (2)$$

where $F(k, \theta)$ is defined such that $\langle\eta^2\rangle = \int F(k,\theta)k\, dk\, d\theta$, η being the sea surface displacement with the angle brackets representing a spatial average; $\mathbf{c}_g$ is the group velocity, $\mathbf{u}_c$ is the surface current velocity; and $S_{\rm in}$, $S_{\rm nl}$, and $S_{\rm ds}$ correspond to the wind input, nonlinear energy transfer, and energy dissipation, respectively. In stationary fetch-limited conditions, Eq. (2) becomes

$$(\mathbf{c}_g + \mathbf{u}_c)\cdot\nabla F(k,\theta) = S_{\rm in} + S_{\rm nl} + S_{\rm ds}. \qquad (3)$$

The wind input $S_{\rm in}$ has been studied extensively both theoretically and empirically from both laboratory and field observations. Miles (1957, 1959) provided a theory describing the generation of waves by wind due to shear-flow instability. The theory predicts a small phase shift between the surface pressure and the surface elevation resulting in a transfer of energy and momentum corresponding to $\langle p\, \partial\eta/\partial x\rangle\, c$ and $\langle p\, \partial\eta/\partial x\rangle$, respectively. Here the angle brackets correspond to a wave phase average, p is the pressure at the surface η, and x is the wind direction.

Plant (1982) collated the available wind wave growth-rate observations from the literature and provided an empirical fit to the growth rate parameter γ, defined by

$$\gamma \equiv S_{\mathrm{in}}(k, \theta_w)/F(k, \theta_w), \tag{4}$$

where θ_w is the wind direction. Subsequently, Janssen (1989, 1991) derived an extension to the Miles theory with a quasi-linear theory that couples the waves and the mean airflow by allowing modifications of the mean wind profile due to wave-induced velocity and pressure fluctuations.

The nonlinear energy transfer due to four-wave resonant interactions has been known in analytical form since the work by Hasselmann (1962, 1963) and Zakharov and Filonenko (1967). It is characterized by a direct and an inverse cascade of energy toward both higher and lower wavenumbers, respectively. As shown by Young and van Vledder (1993), the nonlinear energy transfer due to four-wave resonant interactions plays an important role in the evolution of the wind wave spectrum downshifting the peak wavenumber and controlling the directional spreading.

In the past, owing to the lack of information about its form, the dissipation function due to wave breaking used in numerical wind wave models has served as the tuning knob to match numerical models to observations. The traditional approach is due to Komen et al. (1984), where the dissipation function is formulated from physical arguments and a few free parameters that are tuned, by trial and error, against field observations under idealized conditions. However, more recent studies (Banner and Morison 2010) have constrained some of the whitecapping parameters based on observations of breaking waves in the field (Banner et al. 2000, 2002). In the present study, the spectral dissipation S_{ds} is solved as a residual from all other terms in Eq. (3) according to

$$S_{\mathrm{ds}}(\mathbf{k}) = S_{\mathrm{ad}} - S_{\mathrm{in}}(\mathbf{k}) - S_{\mathrm{nl}}(\mathbf{k}), \tag{5}$$

where S_{ad} is the advective term on the left-hand side of Eq. (3). The right-hand side of Eq. (5) is calculated using the measured directional wavenumber spectra, their spatial gradients, turbulent fluxes from GOTEX, several parameterizations of S_{in}, and exact computations of the nonlinear energy transfer due to four-wave resonant interactions. The stationarity assumption in Eq. (5) for this study is justified by the fact that the GOTEX data were shown to agree with the classical fetch relations (Romero and Melville 2010a), which supports the assumption that the data were collected under approximately stationary fetch-limited conditions.

Since the GOTEX observations did not collect surface current data, in this study wave energy advection is approximated by $S_{\mathrm{ad}} = \mathbf{c}_g \cdot \nabla F(k, \theta)$. The data used for this study were collected at short fetches and within the core of the wind jet; thus, it is expected that the surface currents are locally homogeneous and purely wind driven. The uncertainty of S_{ad} associated with the lack of surface current data is described and quantified in appendix B, neglecting any horizontal current gradients. This is justified by the measurements of the sea surface temperature (SST) in the sampling area of this study, which showed very weak SST gradients, suggesting that the horizontal shear of the surface currents is small. However, as discussed in Melville et al. (2005), the observed whitecap coverage near sharp SST fronts showed substantial variability over short spatial scales. Thus, it is important for future field studies of wave breaking near fronts to have good information about the underlying surface currents with good spatial resolution.

Some of the earliest studies of the energy dissipation due to wave breaking are by Duncan (1981, 1983). He performed laboratory experiments with quasi-steady breakers created by a submerged hydrofoil and showed that the energy dissipation rate per unit length ϵ_l scaled according to

$$\epsilon_l = \frac{b\rho_w c^5}{g}, \tag{6}$$

where b is the empirical breaking parameter, ρ_w is the density of water, g is gravity, and c is the wave phase speed. However, this scaling is already implicit in the scaling of the wave making power of a submerged cylinder moving orthogonally to its axis (Lighthill 1978, p. 459). Phillips (1985) developed a model for the equilibrium part of the spectrum of wind-generated waves and assumed that b was a constant in order to infer the wave breaking statistics from Eq. (1). Other recent studies have estimated b from the field observations by assuming that b is a constant across the spectrum (Phillips et al. 2001; Gemmrich et al. 2008). However, as shown by the nondimensional scaling in Melville (1994) and recent laboratory experiments by Banner and Peirson (2007) and Drazen et al. (2008), the breaking parameter b is not constant. Its magnitude depends on the wave slope and the bandwidth of the focusing packet or on the rate of energy convergence at the center of the breaking wave group (Banner and Peirson 2007). As shown in Fig. 1, the magnitude of b can vary over three orders of magnitude. Thus, it is expected that b is not a constant across the wind wave spectrum but rather a spectral function $b(k)$, with a parametric dependence on wave slope, wave age, and other parameters characterizing the wave field. The recent model by Banner and Morison (2010) also recognized the dependence of b on the scale of the waves, but their predictions of b were limited to the peak of the spectrum, namely, $b(k_p)$.

3. The semiempirical model

The Gulf of Tehuantepec Experiment in February 2004 collected airborne measurements of waves and wind in strong offshore wind conditions. The instruments included the Airborne Topographic Mapper (ATM), which is a conical scanning lidar to measure the sea surface displacement as a function of two horizontal dimensions and time, a fixed lidar (Riegl) to measure the surface displacement along a single cut through the wave field, video imagery of the sea surface to detect and measure the kinematics and length of breaking fronts (Kleiss and Melville 2010, 2011), and a high-frequency radome pressure sensor array to measure the turbulent atmospheric fluxes (Romero and Melville 2010a).

The ATM measurements provided two-dimensional wavenumber spectra with an upper wavenumber limit $k_m = 0.35$ rad m^{-1}, before reaching the noise floor (Romero and Melville 2010a). However, the fixed lidar measurements provided orthogonal one-dimensional wavenumber k_1 and k_2 spectra with k_1 approximately aligned with the local winds, covering a wider range of wavenumbers, with an upper wavenumber limit of 2 rad m^{-1}. The fixed lidar measurements showed that at sufficiently high wavenumbers the directional spectrum is consistent with an isotropic form with $F(k,\theta) \approx \overline{B}\pi^{-1}k^{-4}$, and the proportionality constant $\overline{B}$ showed little or no dependence on the external forcing, in good agreement with the observations by Banner et al. (1989) at much higher wavenumbers.[1] To close the energy equation [Eq. (3)] and momentum budgets, as well as to compute the nonlinear energy fluxes due to four-wave resonant interactions, the measured directional spectra were extrapolated to large wavenumbers with an upper limit of 20 rad m^{-1}, as described below.

a. Spectral grid and extrapolation

The algorithm used to calculate the nonlinear energy transfer due to four-wave resonant interactions, developed by Resio and Perrie (1991), requires a polar grid with a constant bandwidth, such that $\delta k/k$ = const, where δk corresponds to the wavenumber resolution of the spectral grid. In this study, the measured ATM spectra were interpolated on a polar grid with a directional resolution of 4.6° and $\delta k/k = 0.0679$ with extrapolation to higher wavenumbers matching both the fixed lidar data at intermediate wavenumbers and the Banner et al. (1989) data at larger wavenumbers.

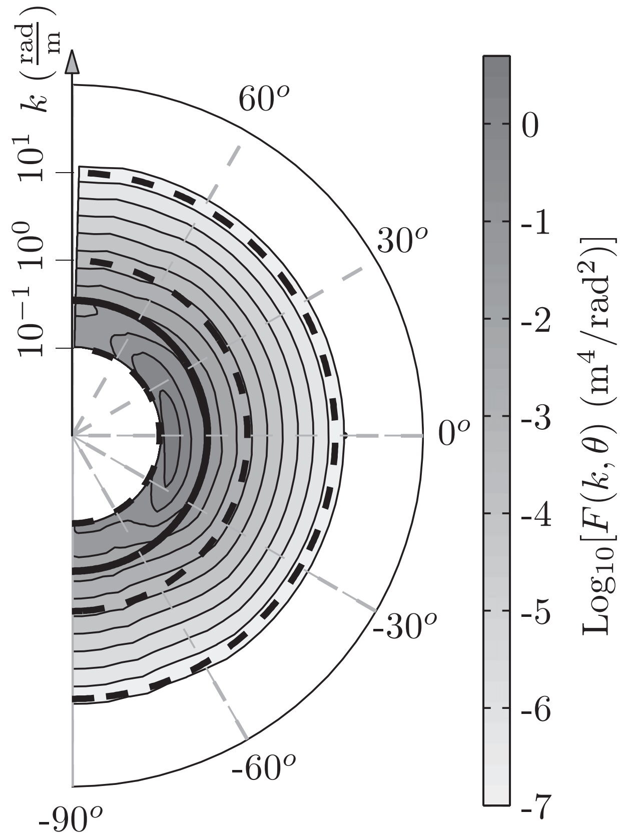

FIG. 2. Sample directional wavenumber spectrum $F(k, \theta)$ with extrapolated tail at large wavenumbers and $\theta = 0°$ corresponding to the direction of the spectral peak. The data were collected during research flight 7 at 15.93°N, 93.13°W during GOTEX. The local wave age $c_p/u_* = 13$. The solid black line indicates the upper wavenumber limit of the ATM data. The black dashed lines show $k = 1 \times 10^{-1}$, 1×10^0, and 1×10^1 rad m^{-1}.

The measured directional wavenumber spectra were extrapolated toward large wavenumbers with two power laws: $k^{-3.5}$ and k^{-4} at intermediate and large wavenumbers, respectively. At intermediate scales, for $k_m < k < k_t(\theta)$, $F(k,\theta) = F(k_m,\theta)(k/k_m)^{-3.5}$, where $k_t(\theta)$ is the wavenumber at which the intermediate wavenumber extrapolation of the spectrum matches the constant saturation regime for which $F(k,\theta) = \overline{B}\pi^{-1}k^{-4}$. Before and after interpolation and extrapolation of the spectrum on a polar grid, it was smoothed to minimize the spectral uncertainty, as described in appendix A.

Figure 2 shows an example of the measured directional wavenumber spectrum $F(k, \theta)$ with extrapolation to 20 rad m^{-1}, with the solid black line indicating the upper

[1] The one-dimensional wavenumber spectra parallel to wind direction reported in MM, extending to about 3 rad m^{-1}, is in excellent agreement with the GOTEX observations (after correcting a processing error of a factor of 2 in MM; see Romero and Melville 2010a), partially filling the gap between the GOTEX observations and Banner et al. (1989).

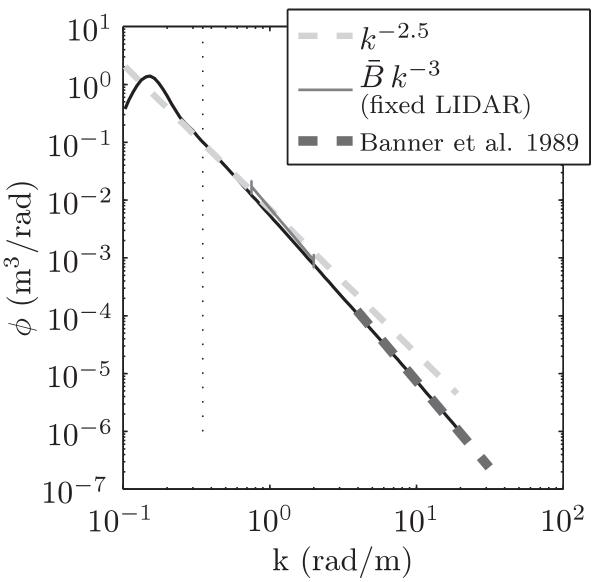

FIG. 3. The solid black line shows a sample omnidirectional spectrum $\phi(k) = \int F(\mathbf{k})k\,d\theta$ with extrapolated tail matching the fixed lidar measurements (dark gray line) and the video stereo observations by Banner et al. (1989) (dark gray dashed line). The light gray dashed line is a reference power law of $k^{-2.5}$. The fixed lidar data show the mean level and standard deviation of the saturation spectrum approximated by an isotropic assumption as $\varphi(k) = \overline{B}k^{-3} \approx k^{-3}(\overline{B_1} + \overline{B_2})/2$ with $\overline{B_1}$ and $\overline{B_2}$ corresponding to the mean saturation in the down wind and crosswind directions, respectively (Romero and Melville 2010a). The data were collected during research flight 7 at 15.93°N, 95.13°W. The local wave age $c_p/u_* = 13$. The vertical dotted line indicates the upper limit of the ATM data.

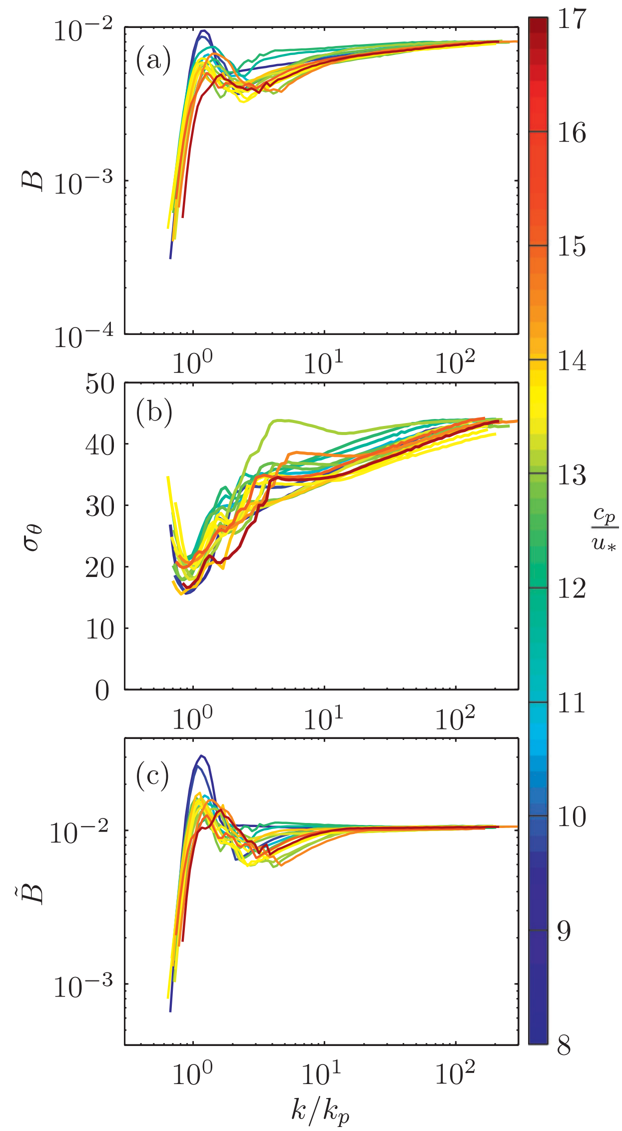

FIG. 4. (a) Azimuth-integrated saturation spectrum $B(k) = \int F(\mathbf{k})k^4\,d\theta$. (b) Directional spreading σ_θ defined in Eq. (8). (c) Normalized saturation $\tilde{B}(k) = B/\sigma_\theta$. The curves are color coded according to the wave age c_p/u_*, where c_p is the wave phase speed corresponding to the wavenumber at the spectral peak k_p and u_* is the friction velocity.

wavenumber cutoff of the measured ATM directional spectrum. There is a smooth transition in the directional distribution from anisotropy, around the spectral peak, to isotropy at large wavenumbers. The same spectrum when integrated in azimuth $\phi(k) = \int F(k, \theta)k\,d\theta$ yields the omnidirectional spectrum shown in Fig. 3. The integrated spectrum also shows a smooth transition between the measured ATM directional spectrum and the extrapolation to large wavenumbers, matching the fixed lidar measurements at intermediate wavenumbers, as well as the observations by Banner et al. at very large wavenumbers. The tail of the composite spectrum can be described by two power laws, $k^{-2.5}$ and k^{-3} at intermediate and large wavenumbers, respectively.

The azimuth-integrated saturation spectrum defined by

$$B(k) \equiv \int F(\mathbf{k})k^4\,d\theta \tag{7}$$

for all composite spectra is shown in Fig. 4a, with the curves color coded according to the wave age c_p/u_*, where c_p is the wave phase speed at the spectral peak k_p and u_* is the friction velocity. The $B(k)$ distributions show a smooth transition toward the constant saturation regime at large wavenumbers. Figure 4b shows the directional spreading $\sigma_\theta(k)$, following Banner and Young (1994), defined by

$$\sigma_\theta(k) \equiv \frac{\int_{-\pi/2}^{\pi/2} F(k,\theta)|\theta|k\,d\theta}{\int_{-\pi/2}^{\pi/2} F(k,\theta)\,d\theta}, \tag{8}$$

where $\theta = 0$ corresponds to the dominant wave direction. The $\sigma_\theta(k)$ curves are narrowest near the spectral peak and are mostly smooth with small kinks at intermediate wavenumbers due to the extrapolation to the high wavenumber tail of $F(k, \theta)$. Finally, Fig. 4c shows a function introduced by Banner et al. (2002) for the characterization of wave breaking, namely, the normalized saturation $\tilde{B}(k)$ defined by

$$\tilde{B}(k) \equiv \frac{B(k)}{\sigma_\theta(k)}. \tag{9}$$

Notice that $\tilde{B}(k)$ is enhanced near the spectral peak k_p when compared to $B(k)$.

b. Wave energy advection

In this study, the wave energy advection $S_{ad} = \mathbf{c}_g \cdot \nabla F$ is approximated by

$$S_{ad} \approx c_g \cos(\theta) \frac{\partial F(k,\theta)}{\partial x}, \tag{10}$$

where $\theta = 0$ corresponds to the dominant wave direction and x is the horizontal distance along the flight track. Equation (10) is based on the assumption that the divergence of energy in the cross-dominant-wave direction is negligible when compared to that in the direction of the dominant waves. This assumption was verified using the numerical simulations of wind wave spectra in GOTEX by Romero and Melville (2010b). The simulations suggest that the approximation in Eq. (10) holds only for the measurements collected near the core of the wind jet and within 100 km of the coast.

Of all measurements from research flights 05, 07, and 10 during GOTEX (Romero and Melville 2010a), there is a total of 16 pairs of measured spectra captured sequentially along the wind jet with a spatial separation of 5–24 km, which, as suggested by the numerical simulations, would satisfy the approximation in Eq. (10). For each of these pairs of measured spectra, S_{ad} was calculated along the dominant wave direction by

$$S_{ad} = c_g \cos(\theta - \theta_p) \frac{F_2(k,\theta) - F_1(k,\theta)}{R/\cos(\theta_R - \theta_p)}, \tag{11}$$

where $F_1(k, \theta)$ and $F_2(k, \theta)$ correspond to the upwind and downwind spectra, respectively; θ_p is the dominant wave direction; and R and θ_R are the displacement and direction, respectively, between each pair of spectra.

c. Nonlinear energy fluxes

The nonlinear energy fluxes due to four-wave resonant interactions S_{nl} were computed with an exact method, Webb–Resio–Tracy (WRT) by Tracy and Resio (1982), which is based on the work by Webb (1978). Specifically, S_{nl} was calculated with the subroutines by van Vledder (2006), who rewrote the WRT method and implemented it in various numerical wind wave models [e.g., WAVEWATCH III and Simulating Waves Nearshore (SWAN)].

d. Wind input and stress partition

The wind input function S_{in} is calculated from the directional spectra and the measured friction velocity u_* using the parameterizations by Snyder et al. (1981) and Janssen (1991) and a modification to Janssen's wind input that, motivated by the work of Chen and Belcher (2000), includes a reduction of the forcing at large wavenumbers due to sheltering induced by the longer waves. As discussed in Romero and Melville (2010a), the calculated profiles of the wind stress reported by Friehe et al. (2006) gave nonzero vertical flux divergence at short fetches, which approximated by a linear relationship suggest an underestimation of the stress by 10%, with an error due to scatter of the data of about 35%. At fetches of 230 km or larger, the data showed negligible vertical flux divergence and scatter of about 1%. Since the data analyzed in this study corresponds to the measurements at short fetches, both the 10-m wind speed and the wind stresses are corrected with a 10% increment in order to account for the observed wind stress divergence.

The empirical wind input function by Snyder et al. (1981) was originally given as a function of the wind speed referenced at 5 m above mean sea level (MSL). Subsequently, the WAMDI Group (1988) adopted the following form of Snyder's wind input in terms of u_*:

$$S_{in}(k,\theta) = \max\left[0, 0.25\frac{\rho_a}{\rho_w}\left(\frac{28u_*}{c}\cos\theta_w - 1\right)\omega F(k,\theta)\right], \tag{12}$$

where ρ_a and ρ_w are the density of air and water, c is the wave speed according to the linear dispersion relationship, and θ_w is the angle between the wind vector and the wave propagation direction.

The wind input by Janssen (1989, 1991) is given by

$$S_{in}(k,\theta) = \frac{\rho_a}{\rho_w}\beta\left(\frac{u_*}{c}\cos\theta_w\right)^2 \omega F(k,\theta), \tag{13}$$

where the Miles parameter $\beta = (\beta_m/u_*)\mu\ \ln^4\mu$ with $\beta_m = 1.2$,

$$\mu = \left(\frac{u_*}{\kappa c}\right)^2 \Omega_m \exp\left(\frac{\kappa c}{u_* \cos\theta_w}\right) \le 1, \tag{14}$$

and $\Omega_m = \kappa g z_o/u_*$ in which $\kappa = 0.4$ is von Kármán's constant and z_o is the roughness length in the air. In this study, z_o is defined by

$$z_o = \frac{\hat{\alpha}\tau}{\rho_a g}\frac{1}{\sqrt{1 - \zeta\tau_w/\tau}}, \tag{15}$$

where $\hat{\alpha} = 0.01$ and $\zeta = 1$ are dimensionless constants, $\tau = \rho_a u_*^2$ is the total stress, and τ_w is the wave-induced stress (i.e., the form drag in the absence of wave breaking) given by

$$\tau_w \equiv \rho_w g \int \cos(\theta_w) \frac{S_{\text{in}}(\mathbf{k})}{c} d\mathbf{k}. \tag{16}$$

Janssen's (1991) wind input formulation from Eqs. (13)–(16) was calculated iteratively for each spectrum as outlined in the following steps. 1) The roughness length is estimated by $z_o = \exp(-U_{10}\kappa/u_*)10$, where U_{10} is the wind speed referenced to 10 m MSL as described in Romero and Melville (2010a); 2) S_{in} is calculated from the directional spectrum and the corresponding measurement of u_* with Eqs. (13) and (14); 3) τ_w and z_o are calculated from Eqs. (16) and (15), respectively; and 4) steps 2 and 3 are repeated up to 10 times to ensure a proper convergence, which was typically achieved in less than four iterations.

The third wind input formulation considered for this study is based on the work by Makin and Kudryavtsev (1999), followed by Chen and Belcher (2000) and Hara and Belcher (2002), in which the longer waves induce a sheltering on the growth of the spectrum at large wavenumbers. Following the approach by Banner and Morison (2010), the sheltering friction velocity $u_*^s(k)$ is defined by

$$u_*^s(k) = \sqrt{\frac{\tau}{\rho_a} - \frac{\rho_w}{\rho_a} g \int_0^{2\pi} \int_{k_l}^{k} \cos(\theta_w) \frac{S_{\text{in}}(\mathbf{k})}{c} d\mathbf{k}}, \tag{17}$$

where k_l corresponds to the lowest wavenumber resolved, and S_{in} is given by

$$S_{\text{in}}(k, \theta) = \frac{\rho_a}{\rho_w} \beta \left[\frac{u_*^s(k)}{c} \cos\theta_w \right]^2 \omega F(k, \theta), \tag{18}$$

corresponding to Janssen's (1991) wind input with added sheltering at large wavenumbers. Note that Eq. (17) differs from that used by Banner and Morison (2010) as it neglects momentum flux induced by wave breaking. The momentum flux supported by separated flow over breaking waves is poorly understood. Recent models (Kudryavtsev and Makin 2007; Mueller and Veron 2009) suggest that it accounts for about 20%–40% of the total momentum flux at wind speeds between 15 and 18 m s^{-1}, corresponding to the range of wind speeds observed in the data used in this study (see Fig. 18).

Equation (18) was calculated iteratively according to the following steps. 1) It is first assumed that $u_*^s(k) = u_*$ and the roughness length is estimated by $z_o = \exp(-U_{10}\kappa/u_*)10$; 2) S_{in} is calculated from the directional spectrum and $u_*^s(k) = u_*$ through Eqs. (18) and (14); 3) τ_w and z_o are calculated from Eqs. (16) and (15); 4) $u_*^s(k)$ is calculated from Eq. (17); and 5) steps 2–4 are repeated up to 100 times to ensure a reasonable convergence, which was typically achieved in less than 30 iterations. The procedure described above was carried out using the same parameters as given for Eq. (13).

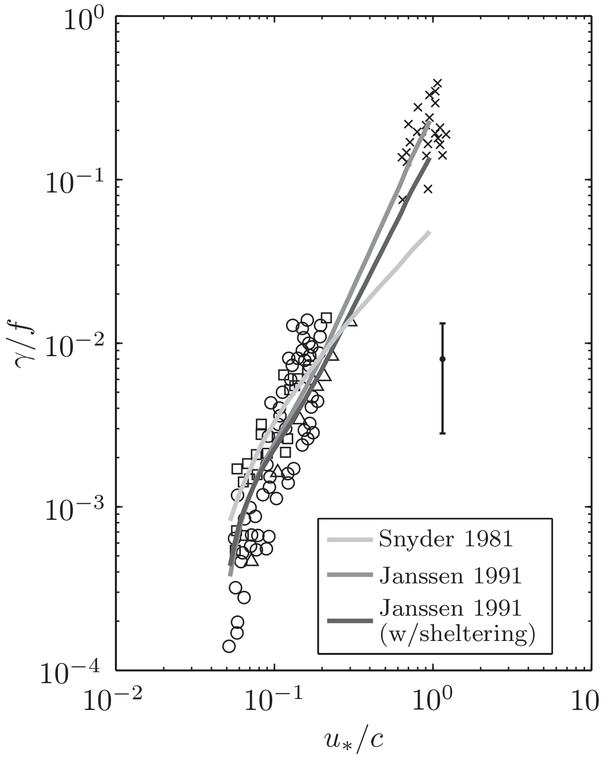

FIG. 5. Dimensionless growth rate γ/f as a function of u_*/c, where $\gamma = S_{\text{in}}(k, \theta_w)/F(k, \theta_w)$, with $S_{\text{in}}(k, \theta_w)$ and $F(k, \theta_w)$ corresponding to the component of the wind input and the energy spectrum, respectively, in the direction of the wind θ_w, and f and c are the wave frequency (Hz) and phase speed according to the linear dispersion relationship. The light gray, gray, and dark gray lines correspond to Snyder et al. (1981), Janssen (1991), and Janssen's sheltered wind input [Eq. (18)], respectively. The symbols show the gravity wave growth data collated by Plant (1982), where both the circles and squares show the field measurements by Snyder et al., whereas the triangles and crosses are the laboratory observations by Shemdin and Hsu (1967) and Wu et al. (1979, 1977), respectively. For error comparison, the bar shows the average error of the data on the strength of breaking b shown in Fig. 14.

Figure 5 shows the dimensionless growth rate γ/f as a function of u_*/c, where $\gamma = S_{\text{in}}(k, \theta_w)/F(k, \theta_w)$, with $S_{\text{in}}(k, \theta_w)$ and $F(k, \theta_w)$ corresponding to the component of the wind input and energy spectra, respectively, in the direction of the wind θ_w and f and c are the wave frequency in Hz and phase speed, respectively, according to the linear dispersion relationship. The light gray, gray, and dark gray lines correspond to Snyder et al. (1981), Janssen (1991), and Janssen's sheltered wind input [Eq. (18)], respectively. The data shown in black symbols correspond to the data

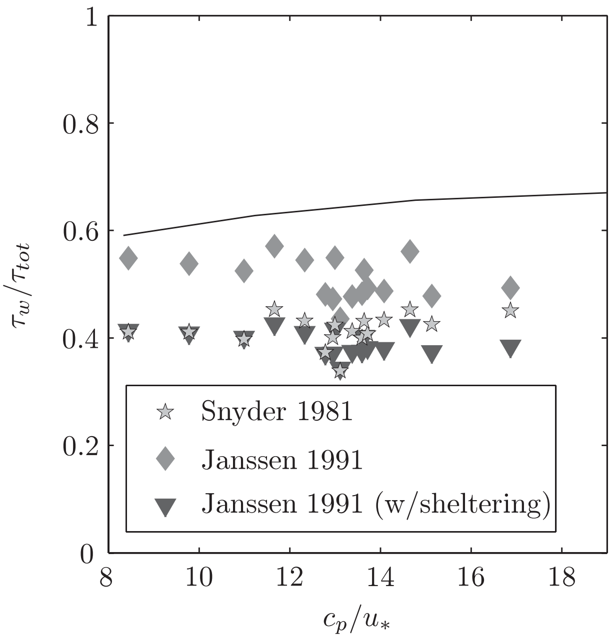

FIG. 6. Ratio of wave-induced momentum flux τ_w to total wind stress τ_{tot} as a function of the local wave age c_p/u_*. The stars, diamonds, and triangles correspond to Snyder et al. (1981), Janssen (1991), and Janssen's sheltered wind input [Eq. (18)], respectively. The solid line corresponds to the modeling results by Banner and Morison (2010), with U_{10} converted into u_* using the drag coefficient from Large and Pond (1982).

collated by Plant (1982), which includes both field and laboratory observations of surface gravity waves.

The parameterization by Janssen gives the lowest forcing for weakly forced waves and the largest growth rate for strongly forced waves. The Snyder forcing is larger than Janssen's for weakly forced waves but much lower than the available data for strongly forced waves. The modification to Janssen's wind input with sheltering at large wavenumbers gave nearly identical results to the original formula without sheltering near the peak with a reduction for the strongly forced or short waves.

The fraction of wave-induced momentum flux τ_w to the total stress τ as a function of the wave age is shown in Fig. 6. The wave-induced momentum flux from the Snyder wind input is in close agreement with the momentum flux due to Janssen's sheltered wind input, being approximately constant at about 50% of the total wind stress.[2] In contrast, the wind input by Janssen (1991) gives

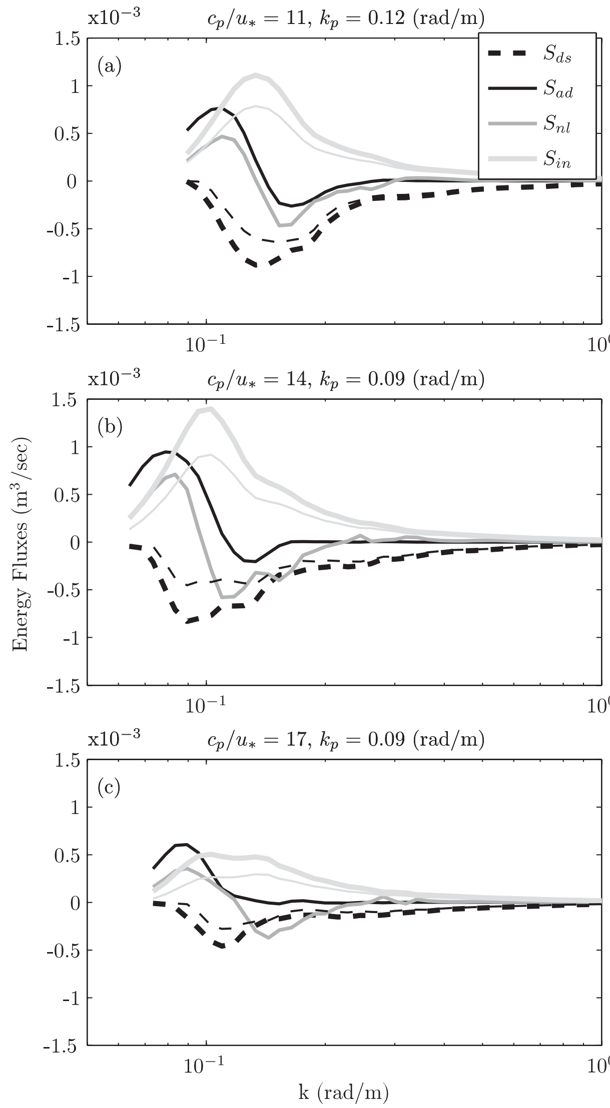

FIG. 7. Sample spectral energy balances at different stages of development. The wave energy advection S_{ad}, nonlinear energy fluxes S_{nl}, and wind input S_{in} are shown with solid black, gray, light gray curves, respectively, and the dissipation S_{ds} is shown with black dashed lines. The wind input and model dissipation shown by the thin and thick lines correspond to the wind input by Janssen (1991) and Snyder et al. (1981), respectively: (a) $c_p/u_* = 11$ in research flight 05, (b) $c_p/u_* = 14$ in research flight 07, and (c) $c_p/u_* = 17$ in research flight 10.

larger values of τ_w and shows a weak reduction of τ_w/τ with increasing wave wage. This trend contrasts with the model results by Banner and Morison (2010) at lower wind speed (12 m s^{-1}). Their results give a weak increase of τ_w/τ with increasing wave age, as shown in Fig. 6 with a solid black line.

e. Spectral energy dissipation

From the spectral energy balance in Eq. (5) three sets of spectral dissipation were calculated from the data,

[2] The ratio τ_w / τ_{tot} reported in Romero and Melville (2010b, Fig. A5) had a scaling error by a factor of 1.56. After correcting this factor, the numerical simulations with the wind input by Snyder (1981) give values slightly larger than those obtained in this study, while the simulations with Yan's (1987) wind input give τ_w / τ_{tot} near unity for the younger waves and approaching 0.8 for older seas.

each corresponding to a different parameterization of $S_{\rm in}$. Figure 7 shows three examples of the spectral energy balance near the spectral peak at different stages of development, with Figs. 7a–c corresponding to $c_p/u_* = 11, 14$, and 17. The wave energy advection $S_{\rm ad}$, nonlinear energy fluxes $S_{\rm nl}$, and wind input $S_{\rm in}$ are shown with solid black, gray, and light gray curves, respectively, and the dissipation $S_{\rm ds}$ is shown with black dashed lines. The wind input and respective dissipation, shown with thin and thick lines, correspond to the semiempirical model with the wind input by Janssen (1991) and Snyder et al. (1981), respectively. Figure 7 shows that all four terms, $S_{\rm ad}$, $S_{\rm in}$, $S_{\rm ds}$, and $S_{\rm nl}$, play significant roles in the energy balance. The nonlinear transfers $S_{\rm nl}$ show the typical three-lobe structure, being negative at intermediate wavenumbers and positive at both low and large wavenumbers.

The calculated wave energy dissipation is based on the balance of the energy transport equation. It is expected that this will correlate with the rate of viscous energy dissipation underneath the breaking waves, reflected in the inertial subrange of turbulence, but equality would only be a special case (cf. Banner and Morison 2010) in an equilibrium situation where the breaking waves are no longer doing work to accelerate the underlying surface currents. Thus, the total breaking wave dissipation may be proportional, but not necessarily equal, to the dissipation rates of turbulence in the water column near the surface.

Since the GOTEX observations did not collect in situ measurements of the energy dissipation, the calculated energy dissipation is compared against the data reported in Thomson et al. (2009) from measurements collected in winds up to 15 m s^{-1}, slightly below the range of wind speeds reported in this study. Figure 8 shows the total dissipation versus the significant slope. This study's estimates of the dissipation are consistent in magnitude with and show similar variability to that reported by Thomson et al. (2009).

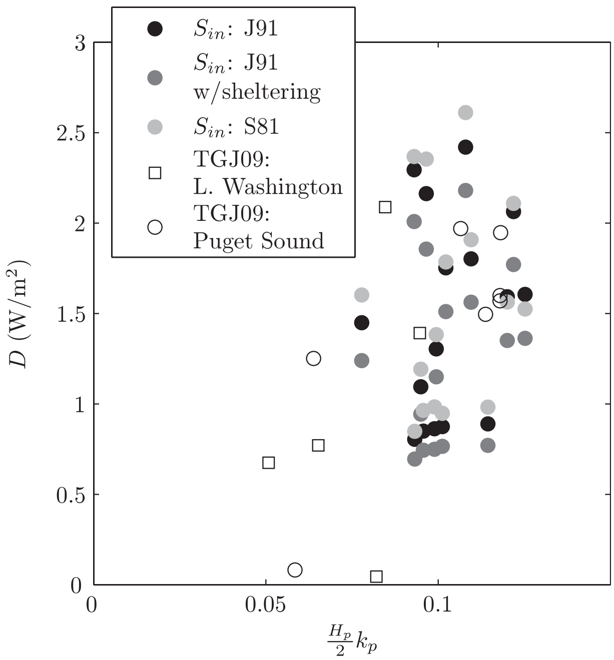

FIG. 8. Energy dissipation rates as function of peak wave steepness $k_pH_p/2$, where $H_p = 4[\int_{.5k_p}^{1.7k_p}\varphi(k)\,dk]^{1/2}$ (Banner et al. 2002). The black, dark gray, and light gray circles show the data with wind input by Janssen (1991), Janssen's sheltered wind input, and Snyder et al. (1981), respectively. The open symbols show in situ measurements of the energy dissipation rates from other field experiments with weaker wind conditions (up to 15 m s^{-1}) reported by Thomson et al. (2009), with the squares and circles corresponding to the data from Lake Washington and Puget Sound. As discussed in section 3e, the wave dissipation and the water-column dissipation rates are generally expected to be proportional but not necessarily equal.

f. Statistics of breaking fronts

Kleiss and Melville (2010) present an analysis of airborne visible video images collected during GOTEX. The video imagery combined with data from the global positioning system (GPS) and an inertial motion unit (IMU) were used to quantify the kinematics and lengths of breakers yielding $\Lambda(\mathbf{c}_{\rm br})$, where $\mathbf{c}_{\rm br}$ is the speed of breaking. In Kleiss and Melville (2010) the measurements of $\Lambda(\mathbf{c}_{\rm br})$ and its moments were analyzed in detail, including its relationship to environmental parameters such as U_{10} and u_* and wave information such as the wave age and wave slope.

Figure 9a shows the azimuth-integrated $\Lambda(c_{\rm br}) = \int\Lambda(c_{\rm br}, \theta)c_{\rm br}\,d\theta$ distributions by Kleiss and Melville (2010) that overlap with the spectra being analyzed in this study. The elemental breaking speed is observed as a function of space and time, with the velocity component normal to the breaking front corrected for the underlying orbital velocity (Kleiss and Melville 2011). The measured $\Lambda(c_{\rm br})$ distributions have a peak at low breaking speeds (2–4 m s^{-1}). At larger values of $c_{\rm br}$, after the peak, the $\Lambda(c_{\rm br})$ distributions show a decreasing trend with increasing speed that differs substantially from the power law of c^{-6} previously suggested by the equilibrium model of Phillips (1985). In Fig. 9b, the breaking speed $c_{\rm br}$ is normalized by c_p and Λ is scaled such that $\Lambda(c_{\rm br}/c_p)d(c_{\rm br}/c_p) = \Lambda(c_{\rm br})dc_{\rm br}$. The distributions of $\Lambda(c/c_{\rm br})$ show a trend with wave age c_p/u_*, generally showing more breaking near the peak of the energy spectrum of younger seas.

During the course of this work it became clear that inclusion of the measured $\Lambda(c_{\rm br})$ distributions for $c_{\rm br}$ near and below their peaks would yield unrealistic values of the breaking function $b(k)$. Moreover, the sensitivity analysis in Kleiss and Melville showed that $\Lambda(c_{\rm br})$ provided the greatest sensitivity to processing method and parameters at lower speeds of breaking, and the $\Lambda(c_{\rm br})$ distributions robustly collapsed for the faster

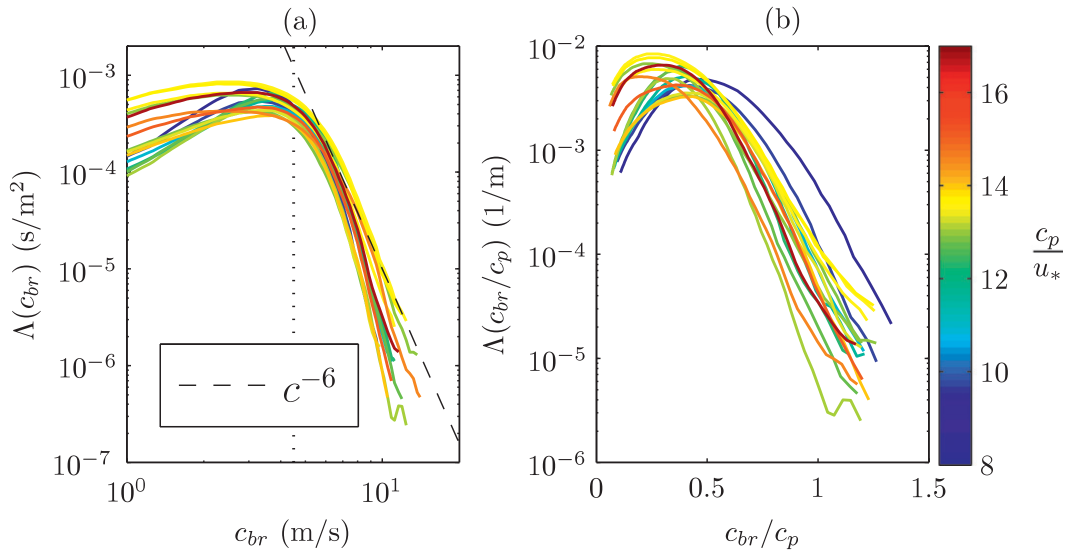

FIG. 9. (a) The $\Lambda(c_{\rm br})$ distributions (Kleiss and Melville 2010) color coded according to the wave age c_p/u_*: the black dashed line is a reference power law of c^{-6} (Phillips 1985) and the vertical dotted line shows $c_o = 4.5$ m s^{-1}, corresponding to the lower limit of the $\Lambda(c_{\rm br})$ data used in this study. (b) The breaking speed $c_{\rm br}$ is normalized by c_p and is scaled by c_p such that $\Lambda(c_{\rm br}/c_p)d(c_{\rm br}/c_p) = \Lambda(c_{\rm br})dc_{\rm br}$.

breaking speeds, giving greater confidence in these observations. Thus, the measurements of $\Lambda(c_{\rm br})$ for $c_{\rm br} < c_o = 4.5$ m s^{-1} were neglected in the calculation of the breaking parameter $b(k)$ described in section 3g. The value of c_o was chosen as a common speed that is after the peak of all the $\Lambda(c_{\rm br})$ distributions (see Fig. 9). A sensitivity analysis (not shown) revealed that the results of this study are not significantly affected by small changes in the chosen value of c_o.

g. *Dimensionless breaking function: b(k)*

As described in section 1, Phillips related the spectral energy dissipation as a function of the wave speed $S_{\rm ds}(c)$ to $\Lambda(c)$ through the breaking parameter b according to Eq. (1). This study is the first attempt to calculate the breaking parameter as a function of k. In the recent modeling work by Banner and Morison (2010), b is implicitly treated as a function of k, but their results are limited to predicting b only at the peak of the spectrum, namely, $b(k_p)$. Solving for b from Eq. (1) gives

$$b(c) = \frac{g^2 S_{ds}(c)}{\Lambda(c)c^5} \tag{19}$$

$$= \frac{g^2 S_{ds}(k)\, dk/dc}{\Lambda(c)c^5}, \tag{20}$$

where $c = \sqrt{g/k}$ is the wave phase speed given by the linear dispersion relationship. As discussed in Kleiss and Melville (2010), available laboratory measurements (Rapp and Melville 1990; Stansell and MacFarlane 2002; Banner and Peirson 2007) have reported a linear relationship between speed of the breaking front and the wave phase speed, namely, $c_{\rm br} = \alpha\, c$, where α is an empirical factor near unity ranging between 0.7 and 0.95. In this study three values of α are considered, 0.8, 0.9, and 1.0, with $\Lambda(c)$ related to $\Lambda(c_{\rm br})$ by

$$\Lambda(c) = \Lambda(c_{br})dc_{br}/dc \tag{21}$$

$$= \alpha\Lambda(c_{br}). \tag{22}$$

Figure 10a shows an example of the $\Lambda(c_{\rm br})$ distributions transformed to $\Lambda(c)$ with $\alpha = 0.9$, and Fig. 10b shows the fifth moment of $\Lambda(c)$.

The sensitivity of the spectral breaking parameter $b(k)$ to small variations in α and the different wind inputs is shown in Fig. 11, with $b(k)$ estimated according to Eq. (20) from model dissipation $S_{\rm ds}(k) = \int S_{\rm ds}(\mathbf{k})k\, d\theta$ and the observed $\Lambda(c)$ distributions (Kleiss and Melville 2010) and converted to the wavenumber domain using the linear dispersion relationship. In Figs. 11a,d,g; Figs. 11b,e,h; and Figs. 11c,f,i, the wind inputs used to calculate the dissipation correspond to Janssen (1991), Janssen (1991) with sheltering, and Snyder et al. (1981), respectively. In Figs. 11a–c, Figs. 11d–f, and Figs. 11g–i, the scaling factor α is 0.8, 0.9, and 1.0, respectively. All nine sets of $b(k)$ show substantial variability, spanning one order of magnitude and, on average, a decreasing trend with increasing wave age. The distributions of $b(k)$ approximately show similar shapes with peaks centered near $k/k_p = 1$. The magnitude of $b(k)$ between the spectral peak and the tail of

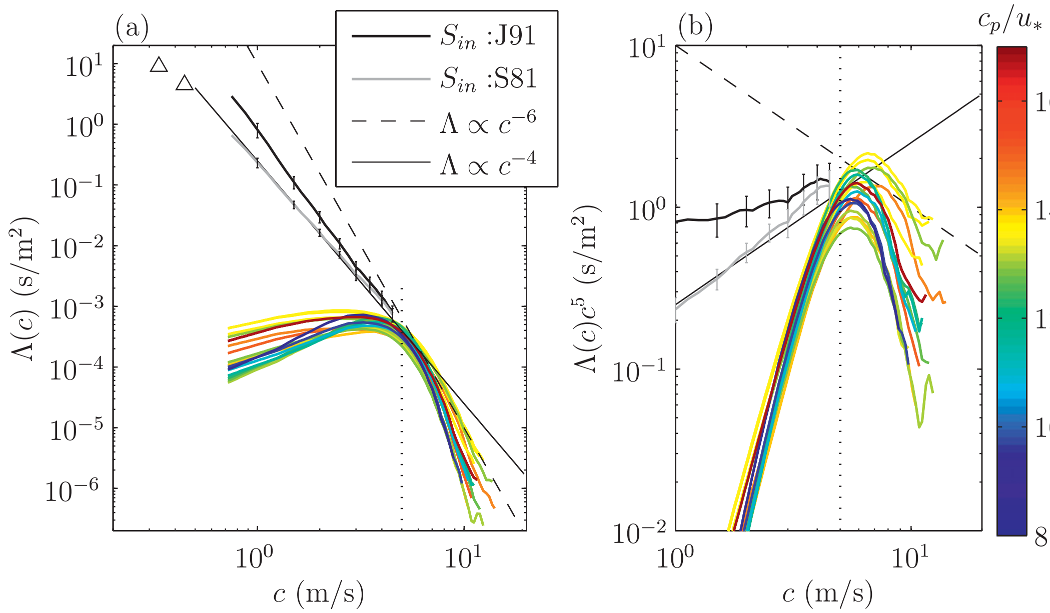

FIG. 10. (a) The $\Lambda(c)$ distributions transformed from wave breaking speed $c_{\rm br}$ to phase speed c according to Eq. (22) with $\alpha = 0.9$. The data are color coded according to the wave age c_p/u_*. The solid colored lines are the video observations by Kleiss and Melville (2010). The black dashed and solid lines are reference power laws of c^{-6} and c^{-4}, respectively. The open triangles correspond to the peak of the $\Lambda(c)$ distributions by Jessup and Phadnis (2005) from laboratory measurements with a wind speed of 9 m s^{-1}, estimated from two different image processing methods. The thick black and gray lines with bars show the bin-averaged predictions of $\Lambda(c)$ based on Eq. (20) and the model $b_2(k)$ (Table 1) and the spectral energy dissipation with wind inputs by Janssen (1991) and Snyder et al. (1981), respectively; the error bars correspond to one standard deviation. (b) As in (a) but with the vertical axis scaled by c^5.

the distribution varies between 1×10^{-4} and 1×10^{-2}, with the wind input by Snyder et al. (1981) giving the largest magnitudes of $b(k)$, with the upper values approaching the average values reported by Thomson et al. (2009) of 1.7×10^{-2} and much larger than those of Gemmrich et al. (2008), $b = 7 \times 10^{-5}$.

Unlike the small variability of $b(k)$ due to the different wind input formulations, the data of $b(k)$ show that the results are very sensitive to small variations in α with the results varying by one order of magnitude for values of α between 0.8 and 1.0. A change of a factor between 5 and 10 is consistent with the predicted change in b from error propagation of Eq. (20), which gives

$$\delta^\alpha b(k) = \frac{\partial b}{\partial \alpha}\delta\alpha = 5\frac{\delta\alpha}{\alpha}b(k),$$

where $\delta^\alpha b(k)$ refers to the uncertainty of $b(k)$ owing to the uncertainty of α, and the factor of 5 arises from the fifth power of c.

To reduce the scatter and the uncertainty of the measured distributions of $b(k)$, the data were bin averaged according to the wave age, yielding three best estimates of $b(k)$ at wave ages centered at $c_p/u_* = 11$, 13, and 15. Following a standard error analysis procedure (Taylor 1997, chapter 7), the bin-averaged data of $b(k)$ were calculated by

$$\sum_{i=1}^{N} w_i(k)b_i(k) \bigg/ \sum_{i=1}^{N} w_i(k),$$

where $w_i(k) = 1/\delta b_i^2(k)$ and the index i refers to the ith observed distribution within a given bin with a total of N observations within each bin ($N \approx 5$).

Figure 14 shows the bin-averaged data of $b(k)$, corresponding to the data in Fig. 11. The bin-averaged data retained a weak trend with wave age, with larger values for younger seas. Despite the data averaging, the errors of $b(k)$ are large, occasionally approaching 100% at large wavenumbers. This is mainly due to the large uncertainty of $\Lambda(c)$ and the reduced number of degrees of freedom at large wavenumbers. The error bars shown correspond to $1/\sqrt{\sum w_i(k)}$. A description of the experimental errors of $\delta b(k)$ is in appendix B.

4. The model of $b(k)$

Several laboratory measurements (Melville and Rapp 1985; Rapp and Melville 1990; Melville 1994; Banner

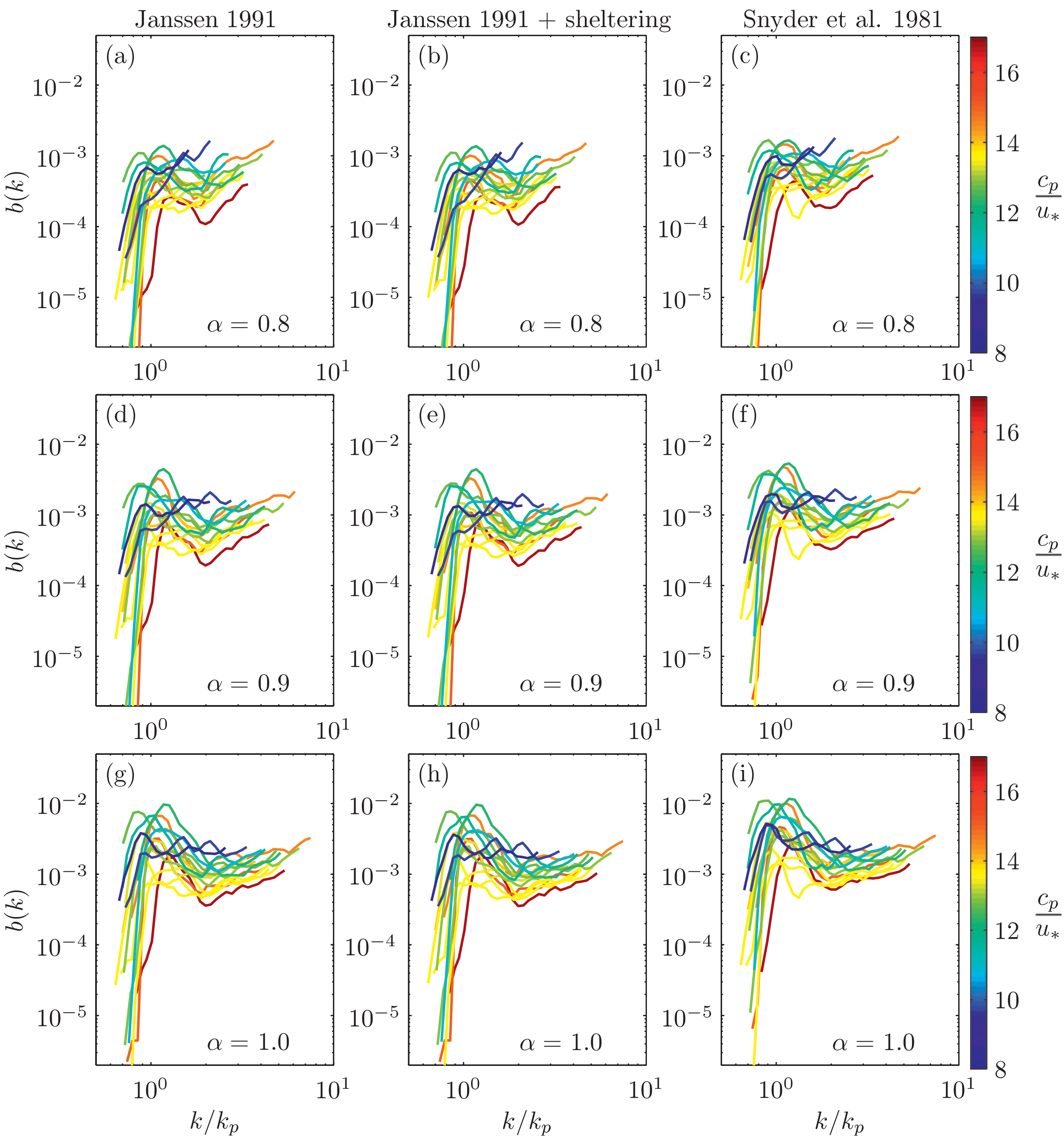

FIG. 11. Spectral strength of breaking $b(k)$ estimated from the model dissipation $S_{ds}(k) = \int S_{ds}(\mathbf{k})k\, d\theta$ and the observed wave breaking statistics $\Lambda(c)$ from Kleiss and Melville (2010). The wind inputs used to calculate the dissipation correspond to (left to right) Janssen (1991); Janssen (1991) with sheltering; and Snyder et al. (1981). The scaling factor $\alpha = c_{br}/c$ relating the breaking speed c_{br} to the phase speed c is (a)–(c) 0.8, (d)–(f) 0.9, and (g)–(i) 1.0. The data are color coded by wave age c_p/u_*.

and Peirson 2007; Drazen et al. 2008) have shown that both energy dissipation and momentum flux associated with wave breaking exhibit threshold behavior. Figure 1 shows available laboratory measurements of the breaking parameter b as a function of the predicted maximum linear slope S of the focusing wave packet, which clearly shows threshold dependence on S, rapidly approaching zero at low values of S. The dashed and solid lines correspond to

$$b(S) = 0.65(S - 0.066)^3 \tag{23}$$

and

$$b(S) = 0.4(S - 0.08)^{5/2}, \qquad (24)$$

respectively, which in Fig. 1 smoothly connect all datasets. The powers of $5/2$ and 3 are consistent with the inertial scaling ($b \propto S^{5/2}$) and measurements ($b \propto S^{2.77}$) of Drazen et al. (2008), while the slope thresholds $S_T = 0.08$ and 0.066 and scaling factors of 0.4 and 0.65 were obtained from a visual fit through the data.

The concept of a wave breaking threshold behavior has been around for many years. Following Longuet-Higgins (1969), Snyder and Kennedy (1983) developed a theoretical model for the formation of whitecaps based on a threshold mechanism of the vertical acceleration. The laboratory experiments by Melville and Rapp (1985) and Rapp and Melville (1990) showed that the loss of excess momentum flux associated with wave breaking exhibits a threshold dependence on the input wave slope ak_c of the focusing wave group, where a is the wave amplitude and k_c is the center wavenumber of the energy spectrum. Banner and Tian (1998) and Song and Banner (2002) studied the onset of breaking from numerical simulations of nonlinear unforced irrotational wave groups and its relationship to the rate of energy convergence at the center of the focusing wave packet. Their results were further confirmed experimentally by Banner and Peirson (2007). The field study by Banner et al. (2000) found a threshold behavior for the probability of breaking depending on the significant spectral peak steepness of the local wind sea $H_pk_p/2$. They concluded that $H_pk_p/2$ is an appropriate parameter for characterizing the nonlinear wave group behavior. Banner et al. (2002) investigated the wave breaking probability for multiple scales using the so-called riding wave removal technique. They reported a threshold behavior of the breaking probability on the spectral saturation $B(k)$ and a common threshold behavior dependent on the normalized saturation $\tilde{B}(k)$ across the different scales analyzed.

Based on the inertial scaling of dissipation in plunging waves (Drazen et al. 2008) and laboratory results (Melville 1994; Banner and Peirson 2007; Drazen et al. 2008), along with the threshold behavior from Eq. (23), the following models of the strength of breaking are proposed:

$$b_1(k) = A_1(B(k)^{1/2} - B_T(k)^{1/2})^{5/2} \qquad (25)$$

and

$$b_2(k) = A_2(\tilde{B}(k)^{1/2} - \tilde{B}_T(k)^{1/2})^{5/2}, \qquad (26)$$

where the exponent of ½ is due to power-law considerations since the spectral saturation is related to the mean-square slope (mss) by $\text{mss} = \int B(k)k^{-1}\,dk$, assuming a constant bandwidth ($dk/k = \text{const}$). The exponent $5/2$ is based on the fit to the laboratory results from Eq. (24).[3] The threshold coefficients B_T and $\tilde{B}_T$, as well as the scaling factors A_n ($n = 1, 2$), were determined by fitting Eqs. (25) and (26) to the data of $b(k)$ while maintaining consistency with Eq. (24) through power-law considerations as described below. The $b(k)$ distributions from Figs. 11d,g and from Figs. 11f,i, which correspond to the model with the Janssen (1991) and Snyder et al. (1981) wind input with $\alpha = 0.9$ and 1.0 were used to fit the parametric models of b_n ($n = 1, 2$). The model of $b(k)$ was also tested with the distributions of $b(k)$ with $\alpha = 0.8$, but the result did not converge with the wind input by Janssen.

Data fitting

The azimuth-integrated saturation is defined by

$$B = a_k^2 k^2 \frac{k}{\delta k},$$

where a_k is the Fourier amplitude corresponding to the wavenumber k and δk is the spectral resolution. It is assumed that the linear focusing slope parameter S, when applied to wind-generated waves, is related to the square root of the saturation through a scaling factor ξ as given by

$$S = \xi_1\sqrt{B} \quad \text{or} \quad S = \xi_2\sqrt{\tilde{B}}, \qquad (27)$$

and similarly

$$S_T = \xi_1\sqrt{B_T} \quad \text{or} \quad S_T = \xi_2\sqrt{\tilde{B}_T}, \qquad (28)$$

where ξ_n ($n = 1, 2$) are empirical factors determined by the data and Eq. (24) as described below.

Substitution of Eqs. (27) and (28) into (24) yields

$$b = 0.4\xi_1^{5/2}(\sqrt{B} - \sqrt{B_T})^{5/2}. \qquad (29)$$

Equating (25) and (29) and solving for A_1 gives

$$A_1 = 0.4\xi_1^{5/2}, \qquad (30)$$

and similarly $A_2 = 0.4\xi_2^{5/2}$, which enforce consistency with the laboratory data.

Visual examination of the data of $b(k)$ in Fig. 11 and the saturation spectra in Figs. 4a,c indicate a net phase shift in the peak of the distributions with both B and $\tilde{B}$ having a maximum just above the spectral peak. Although it would be expected that the peak of $b(k)$ correlates with the

[3] The exponent of $5/2$ is consistent with the inertial scaling by Drazen et al. (2008) in Eq. (24).

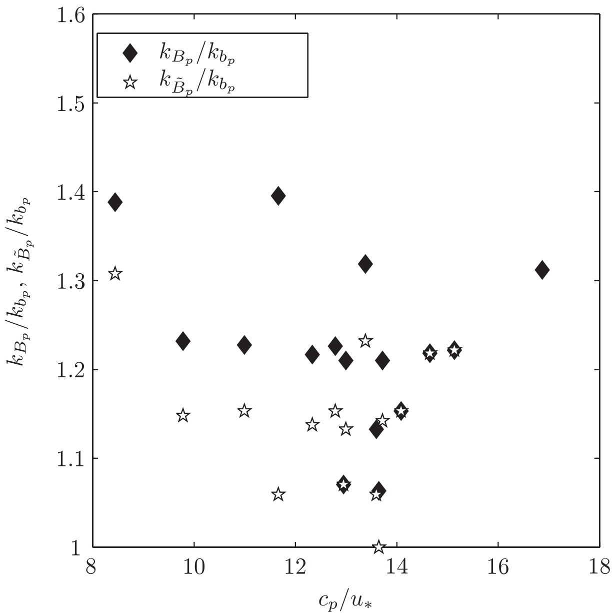

FIG. 12. Wavenumber at the peak of $B(k)$ and $\tilde{B}(k)$, defined as k_{B_p} and $k_{\tilde{B}_p}$, respectively, normalized by the wavenumber at the peak of $b(k)$, k_{b_p}, against the wave age c_p/u_*. The data of k_{b_p} was calculated with $\alpha = 1.0$ and the Snyder et al. (1981) wind input. Results for other values of α (0.8 and 0.9) were very similar and, thus, not shown.

peak of either $B(k)$ or $\tilde{B}(k)$ shifting to larger wavenumbers with increasing wave age, the peaks of the $b(k)$ data are nearly centered at $k/k_p = 1$ and show considerable horizontal scatter. This lack of correlation of the wavenumber at the peak of $b(k)$ with increasing wave age may be associated with the uncertainties of the spectrum at low wavenumbers. As discussed in appendix B, the directional resolution of the measured spectra $\delta\theta$ is inversely proportional to k owing to the conversion of the measured spectra with a finite Cartesian grid to polar coordinates. Moreover, the accuracy of the calculations of $b(k)$ at wavenumbers below the spectral peak are also expected to be affected by the presence of opposing swell, which, although partially removed, has some of its energy wrapped up with the wind sea part of the spectrum because of the 180° ambiguity inherent in spatial Fourier transforms.

Figure 12 shows the wavenumber at the peak of $B(k)$ and $\tilde{B}(k)$, defined as k_{B_p} and $k_{\tilde{B}_p}$, normalized by the wavenumber at the peak of $b(k)$, k_{b_p}, plotted against the wave age. The data shows no trend with wave age, with mean values of 1.3 and 1.2 for k_{B_p}/k_{b_p} and $k_{\tilde{B}_p}/k_{b_p}$, respectively.

To improve the saturation based models $b_1(k)$ and $b_2(k)$, prior to fitting the free parameters of the models, the wavenumber of $b(k)$ and both saturation functions $B(k)$ and $\tilde{B}(k)$ are scaled by the wavenumber at the mode of their distributions. Figure 13 shows examples of $b(k/k_{b_p})$ all having peaks centered at $k/k_{b_p} = 1$. Below, we describe the fitting procedure of the breaking models, carried out after alignment of the peaks of the distributions. For brevity, the normalization factors k_{b_p}, k_{B_p}, and $k_{\tilde{B}_p}$ in $b(k/k_{b_p})$, $B(k/k_B)$, and $\tilde{B}(k/k_{\tilde{B}})$, respectively, will be dropped and the normalized spectral functions will be referred to as $b(k)$, $B(k)$, and $\tilde{B}(k)$.

Parameters A_1 and B_T in Eq. (25) were calculated from the data in Figs. 14d,f and Figs. 14g,i with the following iterative procedure:

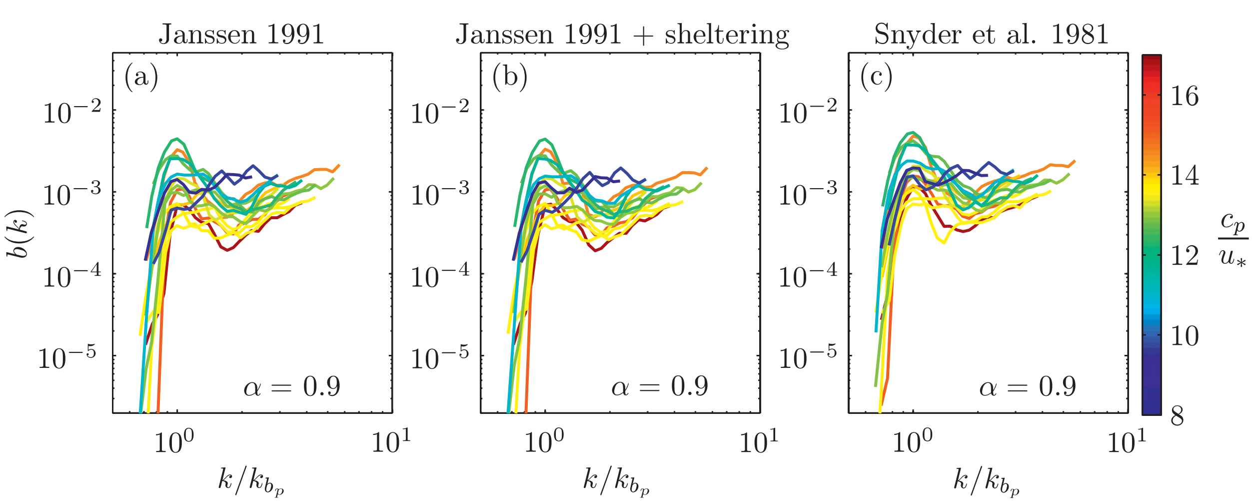

FIG. 13. Spectral strength of breaking $b(k)$ estimated from the semiempirical dissipation $S_{ds}(k) = \int S_{ds}(\mathbf{k})k\,d\theta$ and the observed wave breaking statistics $\Lambda(c)$ from Kleiss and Melville (2010). The horizontal axis is normalized by k_{b_p}, which is the wavenumber at the peak of $b(k)$. The wind inputs used to calculate the dissipation correspond to Janssen (1991), Janssen (1991) with sheltering, and (c) Snyder et al. (1981). The scaling factor $\alpha = c_{br}/c$ relating the breaking speed c_{br} to the phase speed c is 0.9. The data are color coded by wave age c_p/u_*.

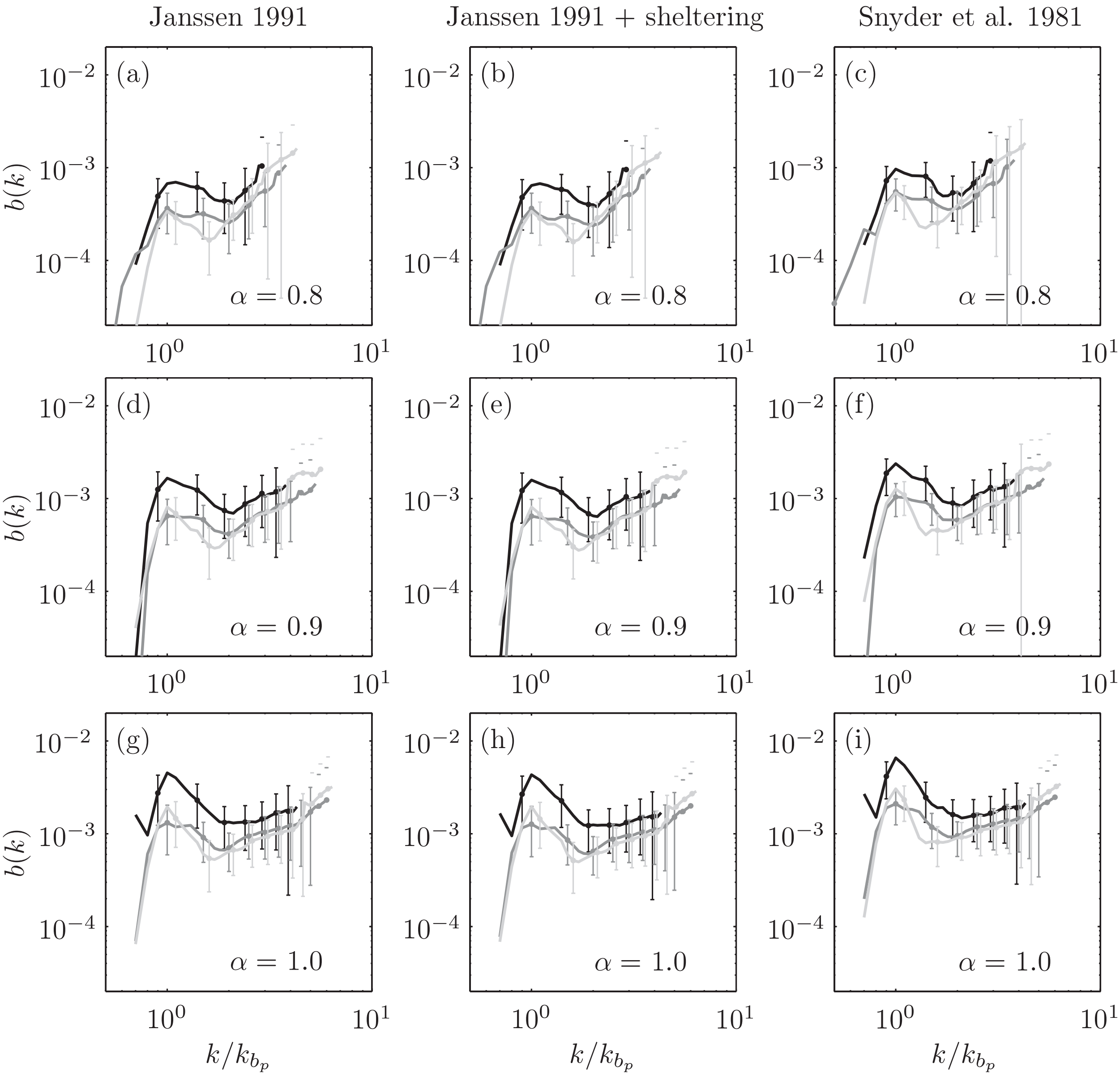

FIG. 14. Bin-averaged spectral strength of breaking $b(k)$ estimated from the model dissipation $S_{\rm ds}(k) = \int S_{\rm ds}(\mathbf{k})k\,d\theta$ and the observed wave breaking statistics $\Lambda(c)$ from Kleiss and Melville (2010). The wind inputs used to calculate the dissipation correspond to Janssen (1991); Janssen (1991) with sheltering; and Snyder et al. (1981). The scaling factor $\alpha = c_{\rm br}/c$ relating the breaking speed $c_{\rm br}$ to the phase speed c is (a)–(c) 0.8, (d)–(f) 0.9, and (g)–(i) 1.0. The data are color coded by wave age c_p/u_*, with the black, dark gray, and light gray lines corresponding to bins centered at $c_p/u_* = 11$, 13, and 15, respectively. The bars show the total error of $b(k)$, which is described in section 3g.

1) It is first assumed that $B_T = 0$.
2) A_1 is calculated by

$$A_1 = \frac{\displaystyle\int_{0.85k_p}^{k_o} b(k)\,dk}{\displaystyle\int_{0.85k_p}^{k_o} (\sqrt{B} - \sqrt{B_T})^{5/2}\,dk}, \quad \text{for} \quad B > B_T, \tag{31}$$

where k_p is the wavenumber at the peak of the energy spectrum and $k_o = g\alpha^2/c_o^2$ is the upper wavenumber limit before the peak in $\Lambda(c)$, according to the linear dispersion relationship.
3) ξ_1 is calculated from A_1 and Eq. (30).
4) B_T is calculated from Eq. (28). Finally steps 2–4 were repeated until reaching convergence, typically in less than 20 iterations. The lower limit in Eq. (31) of $0.85k_p$ provides a sufficiently wide range of wavenumbers

TABLE 1. Average and standard deviation of the parameters of models $b_1(k)$ and $b_2(k)$ in Eqs. (25) and (26) fitted against the bin-averaged data of $b(k)$. The mean and standard deviation values given correspond to the mean and standard deviation of the parameters fitted for each bin-averaged distribution of $b(k)$.

Parameter	Avg ($\alpha = 0.9$)	Std dev ($\alpha = 0.9$)	Avg ($\alpha = 1.0$)	Std dev ($\alpha = 1.0$)
Janssen (1991)				
A_1	3.6	0.4	4.5	0.2
B_T	11.1×10^{-4}	1.0×10^{-4}	9.3×10^{-4}	0.3×10^{-4}
N_{w_1}	5.8	0.5	6.9	0.2
A_2	1.6	0.2	2.1	0.1
$\tilde{B}_T$	2.1×10^{-3}	0.2×10^{-3}	1.7×10^{-3}	0.1×10^{-3}
N_{w_2}	3.0	0.3	3.7	0.2
Snyder et al. (1981)				
A_1	4.0	0.4	5.0	0.2
B_T	10.2×10^{-4}	0.9×10^{-4}	8.5×10^{-4}	0.3×10^{-4}
N_{w_1}	6.3	0.5	7.5	0.2
A_2	1.8	0.2	2.3	0.1
$\tilde{B}_T$	2.0×10^{-3}	0.2×10^{-3}	1.6×10^{-3}	0.1×10^{-3}
N_{w_2}	3.3	0.3	4.1	0.2

while preventing the uncertainties of the data at low wavenumbers. Finally, the algorithm described above was also used to fit the parameters A_2 and $\tilde{B}_T$ in Eq. (26) to the data in Figs. 11d,f,g,i.

The mean results from the fitting algorithm, which is the average of the three cases at different wave ages, are shown in Table 1. Both scaling factors A_1 and A_2 are of order unity, varying between 3.6 and 5.0 and between 1.6 and 2.3, respectively. The mean threshold saturation parameters B_T and $\tilde{B}_T$, varying between 8.5×10^{-4} and 1.1×10^{-3} and between 1.6×10^{-3} and 2.1×10^{-3}, respectively, are low when compared to those obtained from the field observations by Banner et al. (2002), where $B_T = 1.1 \times 10^{-3}$ and $\tilde{B}_T = 4.5 \times 10^{-3}$. The saturation values reported by Banner et al. (2002) may be larger because in fact the measured probability of breaking should go to zero as the saturation approaches a given threshold. Also, as the probability goes to zero, the record length becomes a significant factor in the robustness of the measured breaking probability as the number of rare events becomes small. Thus, the measured threshold saturation from field observations of the breaking probability will always be larger than the "true" saturation threshold.

Comparisons between the bin-averaged data of $b(k)$ and the models b_1 and b_2 with parameters in Table 1 are shown in Figs. 15 and 16, with α equal to 0.9 and 1.0, respectively. The black dashed line is the bin-averaged data and the dark and light dashed lines are models b_1 and b_2, respectively. The data and the model are in good agreement and mostly within error bars, with the model b_1 giving the best agreement for $\alpha = 0.9$ and b_2 when $\alpha = 1$.

5. Discussion

The results presented on the measured spectral strength of breaking $b(k)$ in section 3g have large errors, with the binned data having on average an uncertainty of 65%. However, as shown in Fig. 5, a 65% uncertainty is not very large when compared to the scatter of the available wind input data and also the laboratory data of b in Fig. 1. Additionally, the measured data of $b(k)$ are limited to wavenumbers in the range $0.5k_p < k < 8k_p$. This range of wavenumbers was motivated partially by the limitations on the measurements of $\Lambda(c)$ at low values of c, being greatly affected by the image processing methods used to compute Λ, such as the image brightness threshold. Moreover, the assumption is also justified by the fact that at small scales, $O(0.1–1.0)$ m in length (Jessup et al. 1997), wave breaking does not produce significant numbers of bubbles and consequently $\Lambda(c)$ cannot be reliably measured with visible imagery. Furthermore, the inclusion of the $\Lambda(c_{br})$ data at low values of c_{br} would yield unrealistic values of b. However, it is expected that the high wavenumber portion of the spectrum not resolved in the present study ($k > k_o = g\alpha^2/c_o^2$, where $c_o = 4.5$ m s^{-1}) contains a significant fraction of the total wave energy dissipation rate and most of the wave momentum flux lost due to breaking. Considering the different wind input parameterizations, the wind input by Janssen (1991), Janssen (1991) with added sheltering, and Snyder et al. (1981), it is estimated from the data that on average 49%, 44%, and 36% of the total energy dissipation, respectively, is carried at large wavenumbers ($k > k_o$), whereas the momentum flux due to wave breaking in the same wavenumber range is on average 75%, 70%, and 58% of the total wave breaking momentum flux, respectively.

Assuming that the model b_2 is applicable for shorter waves, using the mean parameters in Table 1 combined with the semiempirical dissipation function in Eq. (5), it is possible to estimate the $\Lambda(c)$ distribution that would close the energy balance in Eq. (19), as shown with thick black and gray lines in Fig. 10, correspond to the model with Janssen's (1991) and Snyder's et al. (1981) wind input, respectively. The power-law behavior of the predictions of $\Lambda(c)$ are consistent with the scaling obtained by balancing the energy wind input to the energy dissipation, assuming a saturated spectrum $\phi \propto k^{-3}$. For a constant value of $b(k)$, $\Lambda(c)$ would scale as c^{-4} and c^{-5}, for the wind input by Snyder et al. (1981) and Janssen (1991), respectively.

It is interesting to note that the predictions of $\Lambda(c)$ at low values of c approximately connect the distributions of visible breakers by Kleiss and Melville (2010) and the available measurements in the literature of microbreaking

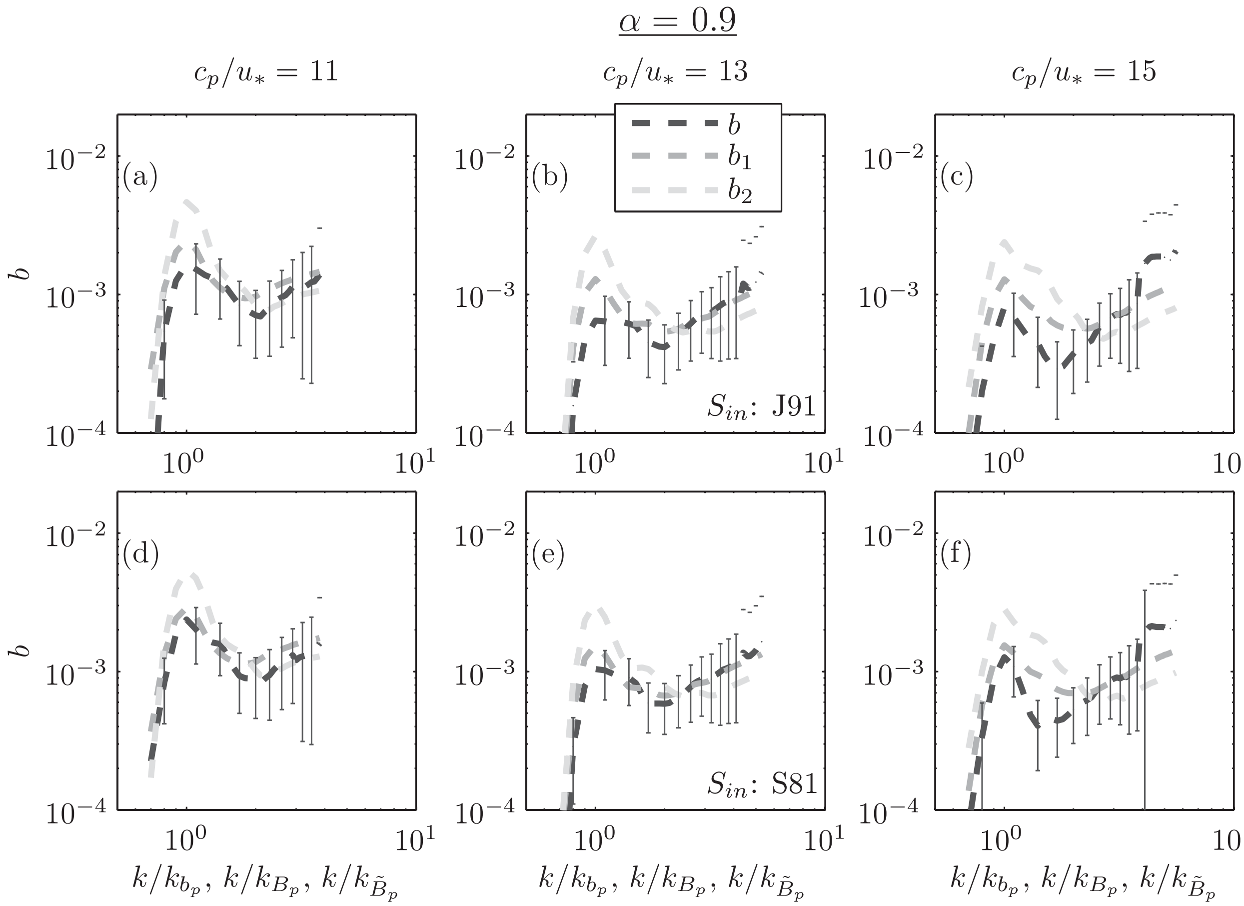

FIG. 15. Fits of the models b_1 and b_2, shown in gray and light gray dashed lines, respectively, compared with the bin-averaged data of $b(k)$, shown with dark-dashed lines. The scaling factor $\alpha = c_{br}/c$ relating the breaking speed c_{br} to the phase speed c is 0.9.

from laboratory experiments in 9 m s^{-1} winds by Jessup and Phadnis (2005). This highlights the need for simultaneous field measurements of $\Lambda(c)$ for both visible and microscale breaking. Figures 17a,b show the spectral breaking strength models b_1 and b_2, respectively. Both models were calculated using the parameters shown in Table 1 with $\alpha = 0.9$. The dashed lines are extrapolations of the models b_1 and b_2 based on $B(k)$ and $\tilde{B}(k)$, respectively. Both models vary substantially near the peak, while converging for $k > 10\ k_p$.

The semiempirical model presented in this study does not explicitly account for momentum flux due to airflow separation from steep or breaking waves or the viscous stress. It is assumed that for a range of conditions the viscous stress does not contribute significantly to wave generation. As shown in Fig. 6, the calculated wave-induced stresses are 40%–80% of the total stress, leaving somewhere between 20% and 60% for viscous and separation stresses, depending on the wind input formulation. Present models in the literature define the momentum flux partition by

$$\tau = \tau_w + \tau_s + \tau_\nu, \tag{32}$$

where τ_w, τ_s, and τ_ν are the wave-induced stress, stress due to airflow separation from breaking waves, and viscous stress, respectively. Figure 18 shows the momentum flux partition in Eq. (32) as a function of wind speed from three recent models in the literature: namely, Kudryavtsev and Makin (2007), Mueller and Veron (2009), and Banner and Morison (2010). Banner and Morison (2010) presented solutions only for 12 m s^{-1} winds, with a momentum flux partition approximately consistent with Kudryavtsev and Makin (2007). At high wind speeds ($U_{10} > 15$ m s^{-1}), the model by Kudryavtsev and Makin predicts a momentum balance with τ_w and τ_s but no viscous stress. Their τ_w is slightly lower than that in this study for wind speeds between 15 and 18 m s^{-1} with Janssen's (1991) sheltered wind input. In contrast, the model by Mueller and Veron (2009) has significant viscous stress even at large wind speeds, giving low values of τ_w that are approximately consistent with this study using Snyder's et al. (1981) wind input. Based on

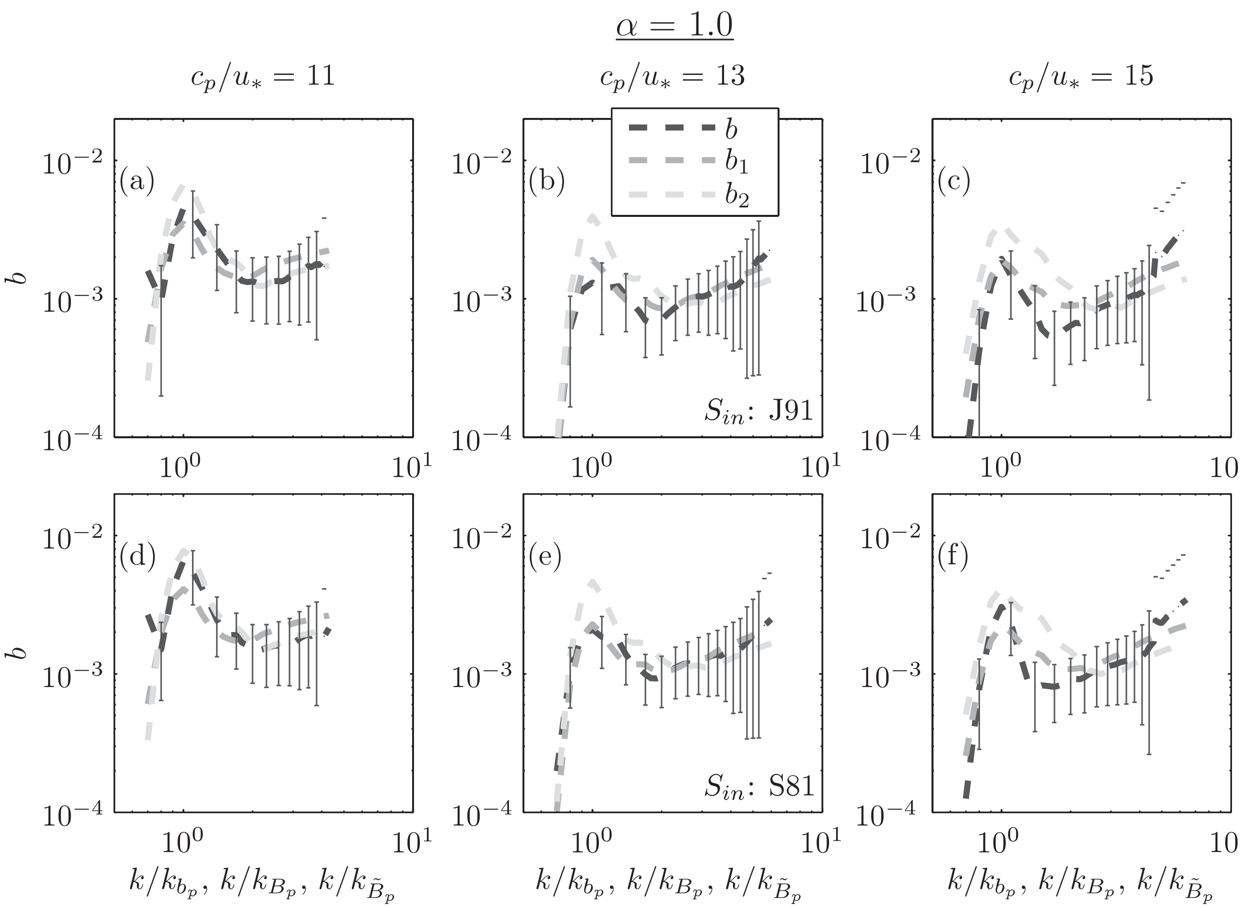

FIG. 16. Fits of the models b_1 and b_2, shown in gray and light gray dashed lines, respectively, compared with the bin-averaged data of $b(k)$, shown with dark gray–dashed lines. The scaling factor $\alpha = c_{\mathrm{br}}/c$ relating the breaking speed c_{br} to the phase speed c is 1.0.

the results from Kudryavtsev and Makin (2007), Mueller and Veron (2009), and Banner and Morison (2010), in appendix B, the uncertainty of the wind input due to the lack of breaking stress has been estimated to be about 20%.

Another aspect that deserves discussion is the physical interpretation of the parameters A_1 and A_2 of the wave breaking strength models b_1 and b_2 in Eqs. (25) and (26), respectively. Here we provide a scaling argument based on the assumption that the ocean is composed of a superposition of self-similar modulated wave groups. Two separate definitions of a spectral background slope, s_{b_1} and s_{b_2} are introduced, one in terms of $B(k)$ and the other as a function of $\tilde{B}(k)$ as given by

$$s_{b_1}(k) \equiv \left(B(k)\frac{\Delta k}{k}\right)^{1/2} \tag{33}$$

and

$$s_{b_2}(k) \equiv \left(\tilde{B}(k)\frac{\Delta k}{k}\right)^{1/2}, \tag{34}$$

where $k^{-1}\Delta k$ is the relative bandwidth of the spectral self-similar wave groups. Then, the expected maximum focusing slope S within each self-similar packet is given by

$$S = s_b N_w, \tag{35}$$

where N_w is the number of waves in a spatial packet or the reciprocal of the relative bandwidth ($k/\Delta k$). By combining Eqs. (27), (30), and (35), with the corresponding definition of the spectral saturation (B or $\tilde{B}$), two relative bandwidth parameters are obtained: $1/N_{w_1} = (A_1/0.4)^{-4/5}$ and $1/N_{w_2} = (A_2/0.4)^{-4/5}$. As shown in Table 1, the results give on average 7 and 4 waves per focusing group, for N_{w_1} and N_{w_2}, respectively. Although this interpretation is largely speculative, it is interesting to note these values for the spatial number of waves in a group

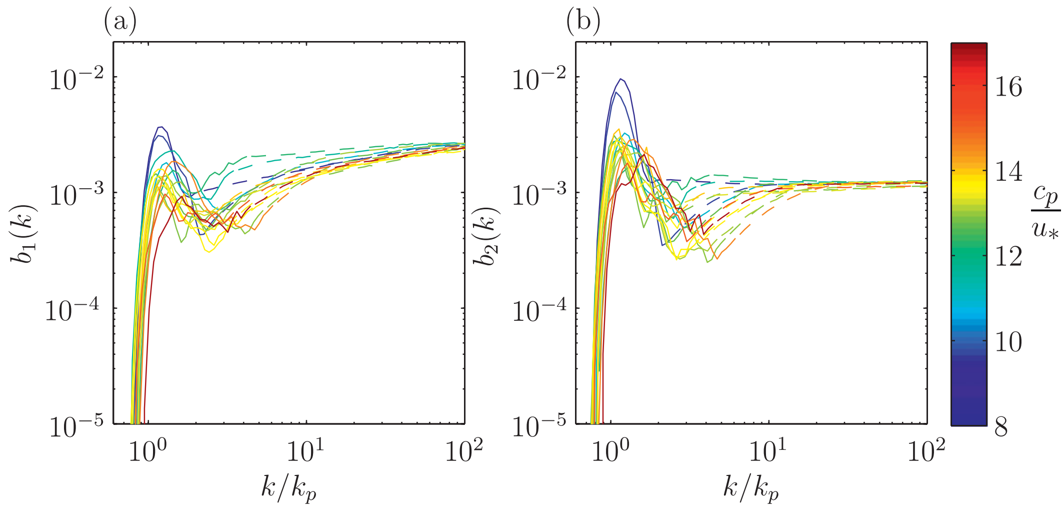

FIG. 17. Spectral breaking strength models (a) b_1 and (b) b_2. Both models were calculated using the parameters shown in Table 1 with $\alpha = 0.9$, and the Janssen (1991) wind input. The dashed lines are extrapolations of the models b_1 and b_2 based on B and $\tilde{B}$, respectively. The data are color coded according to the wave age c_p/u_*.

are qualitatively consistent with the narrowband statistical theory of wave groups by Longuet-Higgins (1984).

Longuet-Higgins [1984, Eq. (4.5)] derived the average number of waves in a group with waves exceeding threshold amplitudes in terms of the spectral bandwidth, which gave good agreement with field observations. The analysis by Longuet-Higgins of temporal field observations gave on average eight waves in a group with wave amplitudes exceeding $2\langle\eta^2\rangle^{1/2}$, which corresponds to four waves per group in the spatial domain. This is qualitatively consistent with the values shown in Table 1.

6. Conclusions

A semiempirical model for the energy dissipation due to wave breaking is presented. The model is based on the radiative transport equation for fetch-limited wind-wave conditions. The model dissipation is estimated from the wave energy advection from measured spectra in the Gulf of Tehuantepec (Romero and Melville 2010a), combined with ‘‘exact’’ computations of the nonlinear energy transfer due to four-wave resonant interactions and three different parameterizations of the wind energy input. Following Phillips (1985), the observed statistics for the length and kinematics of breaking fronts (Kleiss and Melville 2010) are combined with the model dissipation to calculate a spectral function $b(k)$ that characterizes the strength of wave breaking. The calculated values of $b(k)$ are within the range of previous measurements in the laboratory, with $b(k)$ mostly between 1×10^{-4} and 1×10^{-2}, but having significant variability across the different scales and strong sensitivity to the assumed value of α, which is the ratio of the speed of the breaking wave front to the linear phase speed.

Based on the laboratory measurements by Melville and collaborators (Melville 1994), Banner and Peirson (2007), and Drazen et al. (2008), in addition to an inertial scaling argument, $b(k)$ is parameterized in two ways: as a function of the spectral saturation $B(k)$ and the saturation normalized by the directional spreading $\tilde{B}(k)$. To better understand the energy and momentum balance across the air–sea interface, it is important for future field studies to collect simultaneous measurements of $\Lambda(c)$ from both visible and microscale breakers, including, if possible, in situ measurements of the upper-ocean currents; water column turbulent dissipation; good broadband measurements of the directional spectrum, including its gradients in both the downwind and crosswind directions; and supporting atmospheric turbulent fluxes.

Acknowledgments. We acknowledge the collaboration of Carl A. Friehe[4] and Djamal Khelif at the University of California, Irvine, in planning and conducting the GOTEX experiments and in help with the analysis of the atmospheric boundary layer data. We are grateful to Allen Schanot, Henry Boynton, Lowell Genzlinger, Ed Ringleman, and the support staff at the NCAR Research Aviation Facility. We thank Bill Krabill, Bob

[4] We dedicate this paper to the memory of our colleague and friend, Carl Friehe, who passed away on 1 September 2011, during revision of this paper for publication. The GOTEX experiment would not have been possible without Carl's experience and dedication to airborne marine atmospheric boundary layer research.

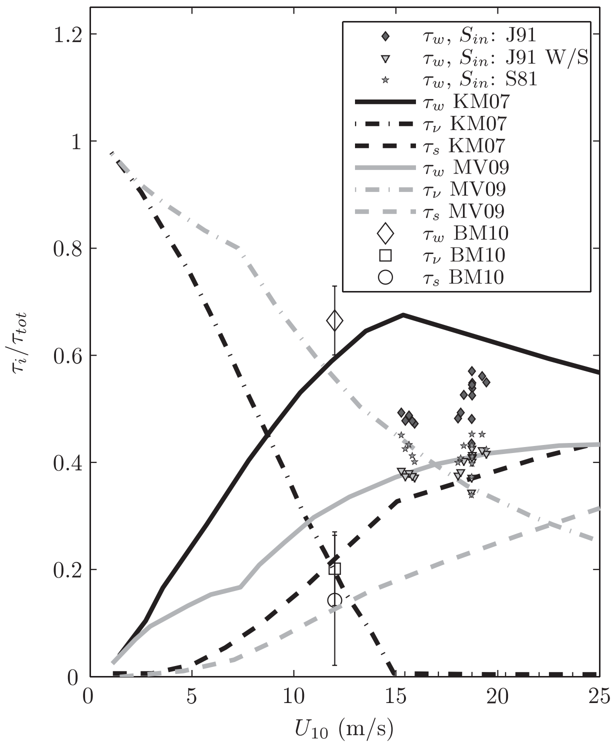

FIG. 18. Stress partition as function of wind speed referenced at 10 m MSL. The closed diamonds, triangles, and stars show this study's wave-induced momentum flux normalized by the total wind stress corresponding to the wind input by Janssen (1991), Snyder et al. (1981), and Janssen's sheltered wind [Eq. (18)], respectively. The wave-induced stress τ_w, viscous stress τ_ν, and stress due to airflow separation from breaking waves τ_s from the models by Kudryavtsev and Makin (2007), Mueller and Veron (2009), and Banner and Morison (2010) are shown with black lines, gray lines, and open symbols, respectively.

Swift, Jim Yungel, John Sonntag, and Robbie Russell at NASA EG&G for access to the ATM, its deployment, and initial data processing. This research was supported by grants to WKM from the National Science Foundation (OCE), the Office of Naval Research (Physical Oceanography).

APPENDIX A

Data Smoothing

The computations of the nonlinear transfer are prone to large errors due to their cubic dependence on the energy spectrum. Thus, it is desirable to have a spectrum with a large number of degrees of freedom (DOF) and thus a small spectral uncertainty. The original wave spectrum has 480 DOF and a spectral uncertainty of 25% of the energy as described in Romero and Melville (2010a). In this study, the spectrum was smoothed, prior to the interpolation on the polar grid, increasing the DOF to 3000, which corresponds to a spectral uncertainty of approximately 5% (Young 1999).

Despite the smoothing of the spectrum prior to the calculation of the various source terms,[A1] the calculated directional wavenumber dissipation occasionally gives values greater than zero. However, further analysis has shown that these errors generally occur at large angles relative to the spectral peak, typically near $|\theta - \theta_p| \approx \pi/4$, and the data confirmed that about 90% of the total dissipation was contained within $|\theta - \theta_p| < \pi/4$. Figure A1 shows an example of the source terms corresponding to the spectrum shown in Figs. 2 and 3. Figures A1a–d show S_{in}, S_{nl}, S_{ad}, and S_{ds}. The gray contours show the area where $S_{\mathrm{ds}} > 0$, which is located at about 45° to the right of the spectral peak, overlapping with an area where $S_{\mathrm{ad}} > 0$, $S_{\mathrm{nl}} < 0$, and S_{in} is rapidly decreasing. According to Eq. (5), this implies that S_{in} is not large enough to balance or exceed $S_{\mathrm{ad}} - S_{\mathrm{nl}}$. This lack of balance is likely due to the asymmetry in the wavenumber plane of S_{ad}, which in turn is induced by the slow rotation of the spectral peak with increasing fetch in the Gulf of Tehuantepec (Romero and Melville 2010a). The dissipation shown in Fig. A1d was obtained by removing the data where $S_{\mathrm{ds}} > 0$ and then filled by interpolation using Gaussian weights. This procedure was repeated with the rest of the data used for the analysis.

APPENDIX B

Error Analysis

The calculation of spectral energy dissipation S_{ds} and the strength of breaking $b(k)$ can have potential errors from various sources such as uncertainty of the energy spectrum, the wind stress error, directional resolution, and the lack of surface current data. Here, we define the uncertainty of S_{ds} by

$$\delta S_{\mathrm{ds}} = (\delta S_{\mathrm{in}}^2 + \delta S_{\mathrm{nl}}^2 + \delta S_{\mathrm{ad}}^2)^{1/2}, \tag{B1}$$

where δS_{ds} is the total error of S_{ds}; δS_{in}, δS_{nl}, and δS_{ad} are the uncertainties in the dissipation due to errors from the wind input, nonlinear fluxes, and advective term. Below, we describe the sources of error for each term on the rhs of Eq. (B1) and calculate the error for S_{ds}.

[A1] Following a reviewer's suggestion, S_{nl} was calculated from the spectrum with and without the additional smoothing. It was determined that S_{nl} was nearly identical between the two sets.

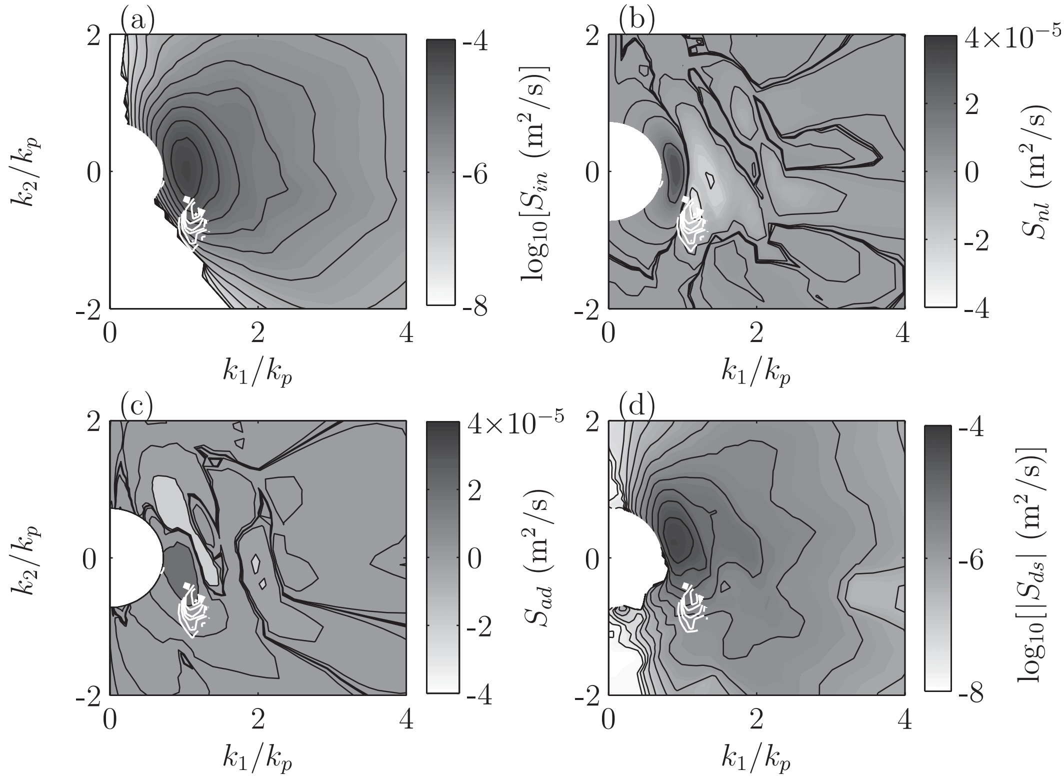

FIG. A1. Terms in the radiative transport equation: (a) S_{in}, (b) S_{nl}, (c) S_{ad}, and (d) S_{ds}. The white contours show the area where $S_{\mathrm{ds}} > 0$. The data shown correspond to the spectrum shown in Figs. 2 and 3.

The uncertainty of the nonlinear energy fluxes δS_{nl} due to the uncertainty of the spectrum δF was calculated directly from the upper and lower error estimates of the spectrum. As expected from the cubic dependence of S_{nl} on the energy spectrum (Phillips 1985), δS_{nl} is approximately $3\delta F = 15\%$: about 14% for the lower and 17% for the upper error bound.

The uncertainties of S_{in} are dominated by the uncertainty of the wind stress, which is 35% based on the uncertainty of the vertical wind stress divergence at short fetches (Romero and Melville 2010a). To leading order, the wind input has a linear dependence on wind stress; thus, the error due to the wind input uncertainty becomes $\delta S_{\mathrm{in}}^{u*} = 0.35 S_{\mathrm{in}}$. Here the uncertainties due to finite directional resolution $d\theta$ are calculated according to

$$\delta S_{\mathrm{in}}^{\theta} = \frac{\partial S_{\mathrm{in}}}{\partial \theta} d\theta = \frac{\partial S_{\mathrm{in}}}{\partial \theta} \frac{0.02}{k},$$

where $d\theta = 0.02/k$ is taken from Eq. (14) in Romero and Melville (2010a) and the value of 0.02 rad m^{-1} corresponds to the resolution of the cross-track wavenumber from the measured spectra (Romero and Melville 2010a). An additional 5% error of the computed wind input is due to the uncertainty of the energy spectrum: namely, $\delta S_{\mathrm{in}}^{F} = 0.05 S_{\mathrm{in}}$. Since the wind input source functions considered for this study do not allow for a modification of the fluxes due to airflow separation over steep breaking fronts, here the uncertainty of the total energy dissipation due to the stress from breaking waves is calculated. The model by Banner and Morison (2010) at winds of 12 m s^{-1} predicts a ratio of wave stress due to breaking waves to total stress of about 15%, whereas the models by Mueller and Veron (2009) and Kudryavtsev and Makin (2007) predict ratios of 20% and 40% for wind speeds of 17 m s^{-1}, respectively (see Fig. 18). Thus, we assume that the uncertainty of the wind input due to the wave breaking stress is roughly 20%.

The advective term has two main sources of error, the finite directional resolution and the lack of surface current information. The propagation of the error of the former gives $\delta S_{\mathrm{ad}}^{\theta} = \tan(\theta) S_{\mathrm{ad}}\, d\theta$. For consistency with the calculation of directional errors from the wind input the directional error is evaluated at $\theta = \pi/4$. Neglecting any horizontal shear, the error due to surface currents is $\delta S_{\mathrm{ad}}^{u_c} = S_{\mathrm{ad}} \delta u_c / c_g$, where the uncertainty δu_c is approximated by the magnitude of the surface currents. The surface current can be approximated as 3% the magnitude of the wind speed (Wu 1975). Thus, for a typical

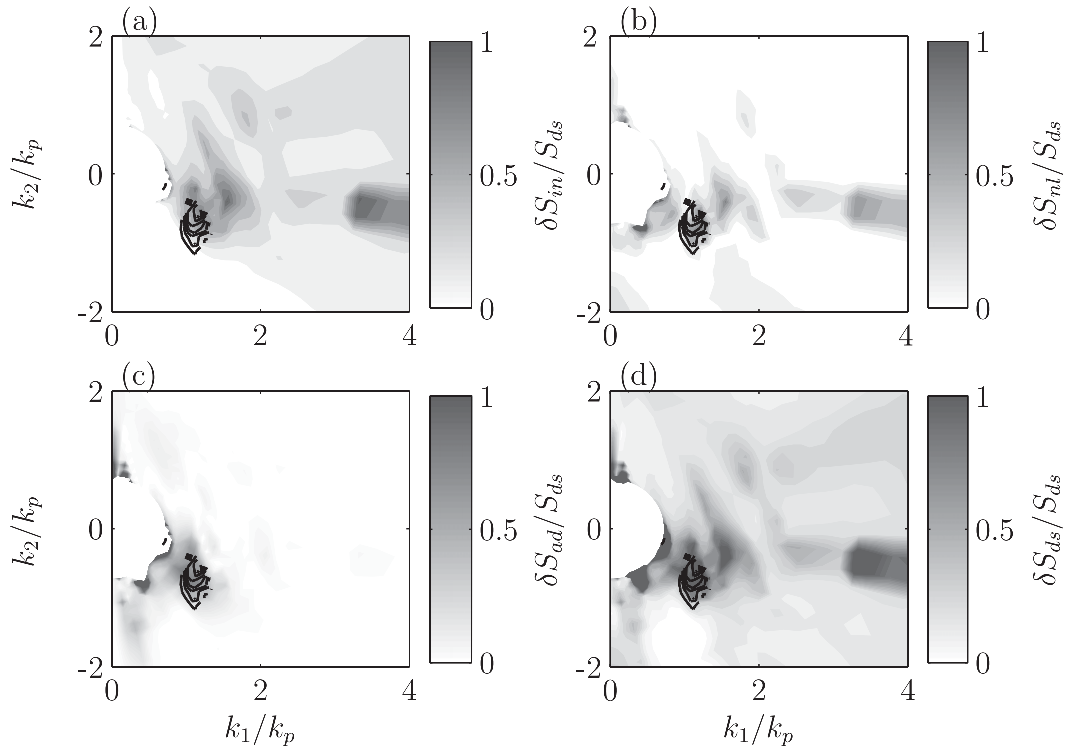

FIG. B1. Uncertainties in the dissipation due to (a) the wind input δS_{in}, (b) the nonlinear energy fluxes δS_{nl}, (c) the advection δS_{ad}, and (d) the energy dissipation δS_{ds}. The error functions shown have been normalized by energy dissipation S_{ds}. Black contours show the area where $S_{\text{ds}} > 0$. The data shown correspond to the spectrum shown in Figs. 2 and 3 and the source term functions shown in Fig. A1.

wind speed of 17 m s^{-1}, the uncertainty $\delta u_c = 0.5$ and the propagation error becomes $\delta S_{\text{ad}}^{u_c} = 0.5 S_{\text{ad}} c_g^{-1}$.

In this study, all of the errors due to S_{ad}, S_{nl}, and S_{in} described above, except the contribution of the airflow separation due to breaking waves, have been computed and added according to Eq. (B1). An example of the directional error functions is shown in Fig. B1, with the error of the wind input (Fig. B1a), nonlinear energy fluxes (Fig. B1b), advection (Fig. B1c), and the energy dissipation (Fig. B1d) normalized by the spectral dissipation. The normalized errors show that the error is largest due to the wind input and that the region of positive dissipation is in regions with large errors in all four source terms.

Finally, the propagation of the error of $b(k)$ [Eq. (19)] gives

$$\frac{\delta b}{b} = \left(\frac{\delta S_{\text{ds}}^2}{S_{\text{ds}}^2} + \frac{\delta \Lambda^2}{\Lambda^2} + 25\frac{\delta c_{\text{br}}^2}{c_{\text{br}}^2}\right)^{1/2}, \tag{B2}$$

where δS_{ds} is given in Eq. (B1), whereas $\delta\Lambda$ and δc_{br} are the experimental errors of Λ and c_{br}, where the large factor in front of the breaker speed error is due to the fifth moment of $\Lambda(c_{\text{br}})$ in Eq. (20). As shown in Kleiss and Melville (2011) (Fig. 5), the uncertainty in $\delta\Lambda(c_{\text{br}})$ is smallest for large values of c_{br} for c_{br} between 4.5 and 10 m s^{-1}. However, within this range of breaker speeds Λ has a strong dependence on c_{br}, giving errors $O(50\%)$. The uncertainty of the breaker speed δc_{br} due to camera motions is 1 m s^{-1}, which produces relative errors, $b^{-1}\delta b = 5c_{\text{br}}^{-1}\delta c_{\text{br}}$, between 110% and 50%, for $c_{\text{br}} =$ 4.5 and 10 m s^{-1}, respectively. Finally, the overall uncertainty δb was calculated according to Eq. (B2) by combining the errors from S_{ds}, Λ, and c_{br}, and is on average about 107% for wavenumbers between the spectral peak and larger.

REFERENCES

Banner, M. L., and I. R. Young, 1994: Modeling spectral dissipation in the evolution of wind waves. Part I: Assessment of existing model performance. *J. Phys. Oceanogr.,* **24,** 1550–1570.

——, and X. Tian, 1998: On the determination of the onset of breaking for modulating surface gravity water waves. *J. Fluid Mech.,* **367,** 107–137.

——, and W. L. Peirson, 2007: Wave breaking onset and strength for two-dimensional deep-water wave groups. *J. Fluid Mech.,* **585,** 93–115.

——, and R. P. Morison, 2010: Refined source terms in wind wave models with explicit wave breaking prediction. Part I: Model framework and validation against field data. *Ocean Modell.,* **33,** 177–189.

——, I. S. F. Jones, and J. C. Trinder, 1989: Wavenumber spectra of short gravity waves. *J. Fluid Mech.,* **198,** 321–344.

——, A. V. Babanin, and I. R. Young, 2000: Breaking probability for dominant waves on the sea surface. *J. Phys. Oceanogr.,* **30,** 3145–3160.

——, J. R. Gemmrich, and D. M. Farmer, 2002: Multiscale measurements of ocean wave breaking probability. *J. Phys. Oceanogr.,* **32,** 3364–3375.

Chen, G., and S. E. Belcher, 2000: Effects of long waves on wind-generated waves. *J. Phys. Oceanogr.,* **30,** 2246–2256.

Drazen, D. A., W. K. Melville, and L. Lenain, 2008: Inertial scaling of dissipation in unsteady breaking waves. *J. Fluid Mech.,* **611,** 307–332.

Duncan, J. H., 1981: An experimental investigation of breaking waves produced by a towed hydrofoil. *Proc. Roy. Soc. London,* **377A,** 331–348.

——, 1983: The breaking and non-breaking wave resistance of a two-dimensional hydrofoil. *J. Fluid Mech.,* **126,** 507–520.

Friehe, C. A., D. Khelif, and W. K. Melville, 2006: Aircraft air–sea flux measurements in the Gulf of Tehuantepec. Preprints, *14th Conf. on Interaction of the Sea and Atmosphere,* Atlanta, GA, Amer. Meteor. Soc., 7.2. [Available online at https://ams.confex.com/ams/Annual2006/techprogram/paper_102500.htm.]

Gemmrich, J. R., M. L. Banner, and C. Garrett, 2008: Spectrally resolved energy dissipation rate and momentum flux of breaking waves. *J. Phys. Oceanogr.,* **38,** 1296–1312.

Hara, T., and S. Belcher, 2002: Wind forcing in the equilibrium range of wind-wave spectra. *J. Fluid Mech.,* **470,** 223–245.

Hasselmann, K., 1962: On the nonlinear energy transfer in a gravity-wave spectrum. Part 1: General theory. *J. Fluid Mech.,* **12,** 481–500.

——, 1963: On the non-linear energy transfer in a gravity wave spectrum. Part 2: Conservation theorems; wave-particle analogy; irreversibility. *J. Fluid Mech.,* **15,** 273–282.

Janssen, P. A. E. M., 1989: Wave-induced stress and the drag of air flow over sea waves. *J. Phys. Oceanogr.,* **19,** 745–754.

——, 1991: Quasi-linear theory of wind wave generation applied to wave forecasting. *J. Phys. Oceanogr.,* **21,** 1631–1642.

Jessup, A. T., and K. R. Phadnis, 2005: Measurement of the geometric and kinematic properties of microscale breaking waves from infrared imagery using a PIV algorithm. *Meas. Sci. Technol.,* **16,** 1961–1969.

——, C. Zappa, and H. Yeh, 1997: Defining and quantifying microscale wave breaking with infrared imagery. *J. Geophys. Res.,* **102,** 23 145–23 153.

Kleiss, J. M., and W. K. Melville, 2010: Observations of wave breaking kinematics in fetch-limited seas. *J. Phys. Oceanogr.,* **40,** 2575–2604.

——, and ——, 2011: The analysis of sea surface imagery for white cap kinematics. *J. Atmos. Oceanic Technol.,* **28,** 219–243.

Komen, G. J., S. Hasselmann, and K. Hasselmann, 1984: On the existence of a fully developed wind-sea spectrum. *J. Phys. Oceanogr.,* **14,** 1271–1285.

Kudryavtsev, V., and V. Makin, 2007: Aerodynamic roughness of the sea surface at high winds. *Bound.-Layer Meteor.,* **125,** 289–303.

Large, W. G., and S. Pond, 1982: Sensible and latent heat flux measurements over the ocean. *J. Phys. Oceanogr.,* **12,** 464–482.

Lighthill, J., 1978: *Waves in Fluids*. Cambridge University Press, 504 pp.

Longuet-Higgins, M. S., 1969: On wave breaking and the equilibrium spectrum of wind-generated waves. *Proc. Roy. Soc. London,* **310A,** 151–159.

——, 1984: Statistical properties of wave groups in a random sea state. *Proc. Roy. Soc. London,* **312A,** 219–250.

Makin, V., and V. Kudryavtsev, 1999: Coupled sea surface–atmospheric model 1. Wind over wave coupling. *J. Geophys. Res.,* **104,** 7613–7624.

Melville, W. K., 1994: Energy dissipation by breaking waves. *J. Phys. Oceanogr.,* **24,** 2041–2049.

——, 1996: The role of surface-wave breaking in air-sea interaction. *Annu. Rev. Fluid Mech.,* **28,** 279–321.

——, and R. J. Rapp, 1985: Momentum flux in breaking waves. *Nature,* **317,** 514–516.

——, and P. Matusov, 2002: Distribution of breaking waves at the ocean surface. *Nature,* **417,** 58–63.

——, L. Romero, and J. M. Kleiss, 2005: Extreme waves in the Gulf of Tehuantepec. *Rogue Waves: Proc. 14th 'Aha Huliko'a Hawaiian Winter Workshop,* Honolulu, HI, University of Hawaii at Manoa, 23–28.

Miles, J. W., 1957: On the generation of surface waves by shear flow. *J. Fluid Mech.,* **3,** 185–204.

——, 1959: On the generation of surface waves by shear flow. Part 2. *J. Fluid Mech.,* **3,** 568–582.

Mueller, J., and F. Veron, 2009: Nonlinear formulation of the bulk surface stress over breaking waves: Feedback mechanisms from air-flow separation. *Bound.-Layer Meteor.,* **130,** 117–134.

Phillips, O. M., 1985: Spectral and statistical properties of the equilibrium range in wind-generated gravity waves. *J. Fluid Mech.,* **156,** 505–531.

——, F. Posner, and J. Hansen, 2001: High range resolution radar measurements of the speed distribution of breaking events in wind-generated ocean waves: Surface impulse and wave energy dissipation rates. *J. Phys. Oceanogr.,* **31,** 450–460.

Plant, W. J., 1982: A relationship between wind stress and wave slope. *J. Geophys. Res.,* **87,** 1961–1967.

Rapp, R. J., and W. K. Melville, 1990: Laboratory measurements of deep water breaking waves. *Philos. Trans. Roy. Soc. London,* **A331,** 735–780.

Resio, D., and W. Perrie, 1991: A numerical study of nonlinear energy fluxes due to wave-wave interactions. Part 1: Methodology and basic results. *J. Fluid Mech.,* **223,** 609–629.

Romero, L., and W. K. Melville, 2010a: Airborne observations of fetch-limited waves in the Gulf of Tehuantepec. *J. Phys. Oceanogr.,* **40,** 441–465.

——, and ——, 2010b: Numerical modeling of fetch-limited waves in the Gulf of Tehuantepec. *J. Phys. Oceanogr.,* **40,** 466–486.

Shemdin, O. H., and E. Y. Hsu, 1967: Direct measurements of aerodynamic pressure above a simple progressive gravity wave. *J. Fluid Mech.,* **30,** 403–426.

Snyder, R. L., and R. M. Kennedy, 1983: On the formation of whitecaps by a threshold mechanism. Part I: Basic formalism. *J. Phys. Oceanogr.,* **13,** 1482–1492.

——, F. Dobson, J. Elliott, and R. B. Long, 1981: Array measurements of atmospheric pressure fluctuations above surface gravity waves. *J. Fluid Mech.,* **102,** 1–59.

Song, J., and M. Banner, 2002: On determining the onset and strength of breaking for deep water waves. Part I: Unforced irrotational wave groups. *J. Phys. Oceanogr.,* **32,** 2541–2558.

Stansell, P., and C. MacFarlane, 2002: Experimental investigation of wave breaking criteria based on wave phase speeds. *J. Phys. Oceanogr.,* **32,** 1269–1283.

Taylor, J. R., 1997: *An Introduction to Error Analysis: The Study of Uncertainties in Physical Measurements*. University Science Books, 327 pp.

Thomson, J., J. R. Gemmrich, and A. T. Jessup, 2009: Energy dissipation and the spectral distribution of whitecaps. *J. Geophys. Res.,* **35,** L11601, doi:10.1029/2009GL038201.

Tracy, B. A., and D. T. Resio, 1982: Theory and calculation of the nonlinear energy transfer between sea waves in deep water. U.S. Army Engineer Waterways Experiment Station Tech. Rep. 11, 54 pp.

van Vledder, G. P., 2006: The WRT method for the computation of non-linear four-wave interactions in discrete spectral wave models. *Coastal Eng.,* **53,** 223–242.

WAMDI Group, 1988: The WAM model—A third generation ocean wave prediction model. *J. Phys. Oceanogr.,* **18,** 1775–1810.

Webb, D., 1978: Non-linear transfers between sea waves. *Deep-Sea Res.,* **25,** 279–298.

Wu, H.-Y., E. Y. Hsu, and R. L. Street, 1977: The energy transfer due to air-input, non-linear wave-wave interactions and white-cap dissipation associated with wind-generated waves. Stanford University Department of Civil Engineering Tech. Rep. 207, 158 pp.

——, E.-Y. Hsu, and R. L. Street, 1979: Experimental study of nonlinear wave-wave interaction and white-cap dissipation of wind-generated waves. *Dyn. Atmos. Oceans,* **3,** 55–78.

Wu, J., 1975: Wind-induced drift currents. *J. Fluid Mech.,* **68,** 49–70.

Yan, L., 1987: An improved wind input source term for third generation ocean wave modelling. Royal Netherlands Meteorological Institute Scientific Rep. WR-87-9, 10 pp.

Young, I. R., 1999: *Wind Generated Ocean Waves*. Elsevier Science, 288 pp.

——, and G. P. van Vledder, 1993: A review of the central role of nonlinear interactions in wind-wave evolution. *Philos. Trans. Roy. Soc. London,* **342A,** 505–524.

Zakharov, V. E., and N. N. Filonenko, 1967: Energy spectrum for stochastic oscillations of the surface of a liquid. *Sov. Phys. Dokl.,* **11,** 881–883.